Exploring controls on the timing of the phytoplankton bloom in western Baffin Bay, Canadian Arctic

Maxime Benoît-Gagné[a,b]*, Stephanie Dutkiewicz[c,d], Inge Deschepper[a,b], Christiane Dufresne[a,b,e], Dany Dumont[f], Raphaël Larouche[b,g], Laurent Mémery[h], Gaëtan Olivier[h], Frédéric Maps[a,b]

[a]Université Laval, Department of Biology, 1045 Av. de la Médecine, Québec, Québec, G1V 0A6, Canada.

[b]Takuvik International Research Laboratory (LRI3376), Université Laval (Canada) - CNRS (France), 1045 Av. de la Médecine, Québec, Québec, G1V 0A6, Canada.

[c]Department of Earth, Atmospheric and Planetary Sciences, Massachusetts Institute of Technology, 77 Massachusetts Avenue, Cambridge, MA 02139, United States of America.

[d]Center for Global Change Science, Massachusetts Institute of Technology, 77 Massachusetts Avenue, Cambridge, MA 02139, United States of America.

[e]Institut Maurice-Lamontagne, Pêches et Océans Canada, 850 route de la Mer, P.O. Boîte 1000, Mont-Joli, QC, G5H 3Z4, Canada.

[f]Institut des sciences de la mer de Rimouski (ISMER), Université du Québec à Rimouski (UQAR), 310 Allée des Ursulines, C.P. 3300, Rimouski, QC, G5L 3A1, Canada.

[g]Université Laval, Department of Biochemistry, Microbiology and Bioinformatics, 1045 Av. de la Médecine, Québec, Québec, G1V 0A6, Canada.

[h]Laboratoire des Sciences de l'Environnement Marin (LEMAR), UBO/CNRS/IRD/Ifremer, Institut Universitaire Européen de la Mer (IUEM), Technopôle Brest-Iroise, Rue Dumont D'urville, 29280 Plouzané, France.

*Corresponding author: maxime.benoit-gagne@takuvik.ulaval.ca

Abstract

In the Arctic Ocean the peak of the phytoplankton bloom occurs around the period of sea ice break-up. Climate change is likely to impact the bloom phenology and its crucial contribution to the production dynamics of Arctic marine ecosystems. Here we explore and quantify controls on the timing of the spring bloom using a one-dimensional biogeochemical/ecosystem model configured for coastal western Baffin Bay. The model reproduces the observations made on the phenology and the assemblage of the phytoplankton community from an ice camp in the region. Using sensitivity experiments, we found that two essential controls on the timing of the spring bloom were the biomass of phytoplankton before bloom initiation and the light under sea ice before sea ice break-up. The level of nitrate before bloom initiation was less important. The bloom peak was delayed up to 20 days if the overwintering phytoplankton biomass was too low. This result highlights the importance of phytoplankton survival mechanisms during polar winter to the pelagic ecosystem of the Arctic Ocean and the spring bloom dynamics.

1 Introduction

Baffin Bay is an important gateway between the Arctic Ocean and the Northwestern Atlantic. Each year during the sea ice retreat, the phytoplankton spring bloom leads to biomass increasing by orders of magnitude, from its lowest values at the end of winter to a peak in summer (Perrette et al., 2011). Because phytoplankton forms the basis of the Arctic marine trophic network (Legendre and Rassoulzadegan, 1995), understanding the controls of the timing of the bloom is critical, especially given the shortness of the productive season. A mismatch between primary and secondary producers in the peak of activity and recruitment may decrease production at the higher trophic levels of the polar marine ecosystems (Søreide et al., 2010; Leu et al., 2011), and even impact the export of organic matter via the biological carbon pump (Henson et al., 2023). The biological carbon pump refers to mechanisms that export organic carbon from the ocean's surface to its interior, where it may be sequestered (Boyd et al., 2019; Henson et al., 2023). Mismatch events have occurred in Arctic environments, but they could increase in frequency and intensity owing to climate change (Søreide et al., 2010). Some of the largest effects of climate change globally occur in the Arctic (Gutiérrez et al., 2021; Rantanen et al., 2022). Moreover, as people living along western Baffin Bay rely partly on subsistence harvest (Kenny and Chan, 2017), unexpected changes in biological production may negatively impact their access to local fishery and marine mammal stocks, and ultimately their food security.

Arctic phytoplankton bloom dynamics are split between three periods separated by two crucial days: the pre-bloom period, the day of the bloom initiation, the growth period, the day of the bloom peak and the post-bloom period (Sakshaug, 2004; Carmack and Wassmann, 2006; Wassmann and Reigstad, 2011). During the pre-bloom period, very low light prevents significant population growth even though nutrient concentrations are high. Snow accumulation allows a transmittance of less than 1% through snow-covered sea ice, but as soon as snow starts to melt transmittance increases to between 2% and 10%, thus allowing the start of the growth period (Ardyna et al., 2020a). For instance, a bloom initiation was detected by floats under 100% sea ice cover as early as February in Baffin Bay (Randelhoff et al., 2020). Data from biogeochemical-Argo floats in the Greenland Sea show that neglecting under-ice blooms would have resulted in the underestimation of the annual net community production of phytoplankton by 52% (Mayot et al., 2018). The controls of the bloom initiation appear to be linked to the optical characteristics of the ice and snow cover, and to the physiological response of phytoplankton to severe light limitation, as was also observed in the Southern Ocean (Hague and Vichi, 2021). The middle of the growth period is associated with melt ponds increasing the proportion of irradiance reaching the water column by up to 25-31%. The growth period ends with the formation of the marginal ice zone when transmittance in the water column reaches 40 to 60%. At this point, the absence of limitation by either light or nutrients produce favourable conditions for exponential growth until the bloom peak is reached (Wassmann and Reigstad, 2011). The initial stock of phytoplankton biomass at the onset of the growth period plays a role in the timing of the bloom peak for the Southern Ocean (e.g., Sakshaug et al., 1991) and the Arctic Ocean (Christian et al., 2022). The post-bloom period follows in response to nutrient depletion and grazing pressure. This period is characterised with a negative or near equilibrium biomass accumulation rate. In the Arctic Ocean, nutrient depletion is thought to exert a stronger control than grazing (Sakshaug, 2004; Randelhoff et al., 2019).

Here we use a complex ecosystem model within an idealised one-dimensional (1-D) water column representative of the conditions in Baffin Bay to better understand the crucial processes controlling the timing of the spring bloom. In particular, we consider the role of light, nutrients and overwintering phytoplankton biomass in the phenology of the spring bloom. Light is thought to control bloom initiation (Ardyna et al., 2020b), while nitrate is the limiting nutrient in Baffin Bay where its eventual decrease is thought to cause the end of the bloom (Randelhoff et al., 2019). The phytoplankton standing stock at the end of the winter is also relevant (Sakshaug et al., 1991; Christian et al., 2022). There remain many questions on how phytoplankton survive over winter. Here we ask how important this survival is to the spring bloom dynamics relative to the other controls. To this end, we conducted sensitivity experiments to better understand and quantify the controls exerted by light, nutrient level and overwintering phytoplankton biomass at the end of winter.

2 Materials and methods

2.1 Ice camp

The model simulations were configured to represent the location of the ice camp of the Green Edge mission in western Baffin Bay at (67.48°N, 63.79°W; Figure 1; see Oziel et al., 2019, for details) that provided rich datasets on oceanographic, biogeochemical and ecological properties of the site (Massicotte et al., 2019; 2020; see Data S3 in Benoît-Gagné et al., 2024). The camp was on seasonal landfast sea ice near Qikiqtarjuaq (Nunavut, Canada) with a water depth of 360 m (Massicotte et al., 2020). It will be referred to as the Qikiqtarjuaq ice camp from here onward. Field observations were collected at the ice camp in 2016 from April 27 to July 22.

During the camp, 134 variables were measured including snow thickness, ice thickness, underwater photosynthetically active radiation (PAR, 400 to 700 nm), nitrate and silicic acid concentrations, chlorophyll a (Chl *a*) and depth of the mixing layer (in both Oziel et al., 2019, and Massicotte et al., 2020). Notations and units mentioned in the main text are described in Table S1. Additionally, there were estimates of the carbon biomass for several plankton taxonomic categories (in both Grondin, 2019, and Massicotte et al., 2020) from an Imaging FlowCytobot (IFCB; Olson and Sosik, 2007; Sosik and Olson, 2007; Moberg and Sosik, 2012; Laney and Sosik, 2014). The IFCB combines microscopy and flow cytometry to produce high-speed images of phytoplankton cells. These images can be used to identify species for cells larger than 10 μm and to identify broader taxonomic groups for cells between 3 μm and 10 μm. Further information is available in Appendix A5.

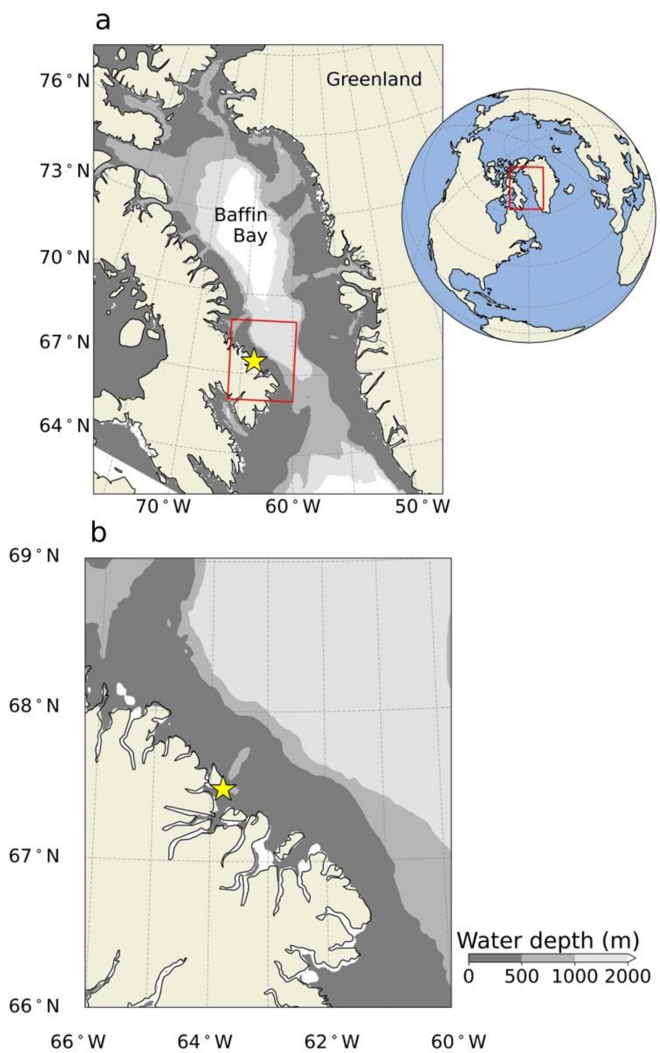

Figure 1. Maps of Baffin Bay and the study site. The yellow star marker represents the Qikiqtarjuaq sea ice camp location (Oziel et al., 2019). a) Map of Baffin Bay. b) Map of the area around the Qikiqtarjuaq sea ice camp (enlarged from the red box in panel a). Bathymetry from Jakobsson et al. (2012; see Data S1 in Benoît-Gagné et al., 2024).

2.2 Numerical model

2.2.1 Model description

The biogeochemical/ecosystem model follows from Dutkiewicz et al. (2021) but was modified here for the Arctic Ocean. We present a brief overview of the simulated functional groups and the size classes. Details can be found in Dutkiewicz et al. (2015; 2020) and Appendix A1. Versions of this ecosystem model have been run and tested in 1-D configurations that were not specific for the Arctic Ocean (Hickman et al., 2010; Wu et al., 2021).

In this study, the numerical planktonic ecosystem included 26 phytoplankton types (Figure 2a) divided into four biogeochemical functional groups, each defined by a few physiological features. Picophytoplankton were the smallest (1.4 μm and 2.0 μm equivalent spherical diameter, *ESD*), diatoms

(6.6–154 μm) required silicic acid, and mixotrophic dinoflagellates (6.6–228 μm) were capable of photosynthesis as well as grazing on other plankton. An additional group of "other nanophytoplankton" were analogs of all other phytoplankton types of similar size that were neither diatoms nor mixotrophic dinoflagellates (for example, haptophytes such as coccolithophores or *Phaeocystis*). The phytoplankton types differed from one another by their maximum growth rate (P^{C}_{max}; Figure 2b) and their half saturation for growth on nitrate (k_{NO_3}; Figure 2c) and were allometrically (i.e., using a relationship between cell size and the parameter) assigned within functional groups (Dutkiewicz et al., 2020; 2021). The half saturation for growth on silicic acid ($k_{Si(OH)_4}$), on phosphate (k_{PO_4}), on iron (k_{Fe}) and on ammonium (k_{NH_4}) for each type was calculated from the corresponding k_{NO_3} as described in Appendix A1.2. The photosynthetic parameters of the model diatom analogs corresponded well to laboratory observations from Arctic diatoms (Figure S1).

Subscript j refers to a specific phytoplankton type and subscript k refers to a zooplankton type. C_j is the biomass of phytoplankton j and Z_k is the biomass of zooplankton k. The source and sinks of the biomass (in carbon) of each phytoplankton type j ($S_{C,j}$) are calculated such that

$$1. \quad S_{C,j} = P^{C}_{max,j}\gamma^{R}\gamma^{T}\gamma^{I}C_j - m_{p,j}\gamma^{T}C_j - \sum_k\left[g_{jk}Z_k\right] - \frac{\delta\omega_{p,j}C_j}{\delta z}.$$

The first right-hand term represents biosynthesis. The limitation for growth by nutrients, temperature and light (γ^R, γ^T, γ^I, respectively) is between 0 (e.g., a lack of light) and 1 (e.g., unlimiting light). The calculations of γ^R, γ^T and γ^I are described in Appendices A1.2, A1.3 and A1.4, respectively. The second term represents the compounded losses of biomass due to respiration, senescence, viral lysis and excretion. The relative impacts of these processes were not resolved individually. Instead, a bulk estimation of these loss processes is calculated from a constant "mortality" rate at 30°C ($m_{p,j}$) of 0.1 d^{-1}. The third term represents grazing (see Appendix A1.5 for the calculation of the grazing rate of j by k, g_{jk}). The fourth term represents the sinking with a constant sinking rate ($\omega_{p,j}$) of 0.07 m d^{-1} for picophytoplankton, 0.36 m d^{-1} for diatoms and 0.23 m d^{-1} for dinoflagellates and other nanophytoplankton. The second and third terms were set to 0 when C_j dropped below a threshold of minimum biomass for phytoplankton j ($C_{min,j}$) of 10^{-2} mmol C m^{-3} to simulate survival in winter. However, sinking and mixing could still dilute the biomass of phytoplankton j below this threshold. The model includes explicit parameterization of Chl *a*, such that each phytoplankton has a dynamic Chl:C ratio that alters due to acclimation following Geider et al. (1997; 1998). For the equations and more details, the reader is referred to Dutkiewicz et al. (2015).

We also consider 16 zooplankton numerical types differing in size, resulting in a marine ecosystem containing a complex planktonic community. The maximum grazing rate of the grazers (g_{max}) depends on their biogeochemical functional group (mixotrophic dinoflagellates or microzooplankton) and their size following an allometric relationship. These g_{max} values are parameterized from the observations by Taniguchi et al. (2014) and Jeong et al. (2010; Figure 2d). The four smallest microzooplankton are an exception, with a g_{max} independent of their size (following a lack of observed allometric relationship between these smallest types, as in Taniguchi et al., 2014).

We used a 1-D configuration representing the specific location of the ice camp in Baffin Bay. The configuration had 75 levels ranging in thickness from 1 m near the surface to 6 m near the bottom (which was 360 m). Temperature, salinity and vertical turbulent diffusivity (K_z) were provided as offline forcing fields. They were generated with a 1-D simulation of the LIM 3.6 sea ice model (Rousset et al., 2015) coupled to the ocean component of the general circulation model NEMO 3.6 (Madec et al., 2017). Hereafter these offline forcing fields will be referred to as NEMO-LIM3 (Data S4 in Benoît-Gagné et al., 2024). The modelled vertical diffusion, K_z was evaluated by comparing with two different metrics of the vertical mixing: the depth of the mixing layer and the depth of the equivalent mixed layer (h_{BD}). The term h_{BD} is the depth of the "buoyancy deficit" as in Randelhoff et al. (2017). The depth of the mixing layer was measured at the ice camp only on June 23, 2016, and corresponded to a K_z around 10^{-4} m^2 s^{-1}. The depth at which $K_z = 10^{-4}$ m^2 s^{-1} was considered as the simulated mixed layer depth herein.

Preliminary experiments revealed that two major adjustments to Dutkiewicz et al. (2021) were required for the Arctic setup: setting a minimum threshold below which phytoplankton experienced no losses, especially during the harsh Arctic winter, and including light under sea ice. The sensitivity experiments that allowed us to choose the best parameters are presented in Sections 3.3 and 3.4, respectively.

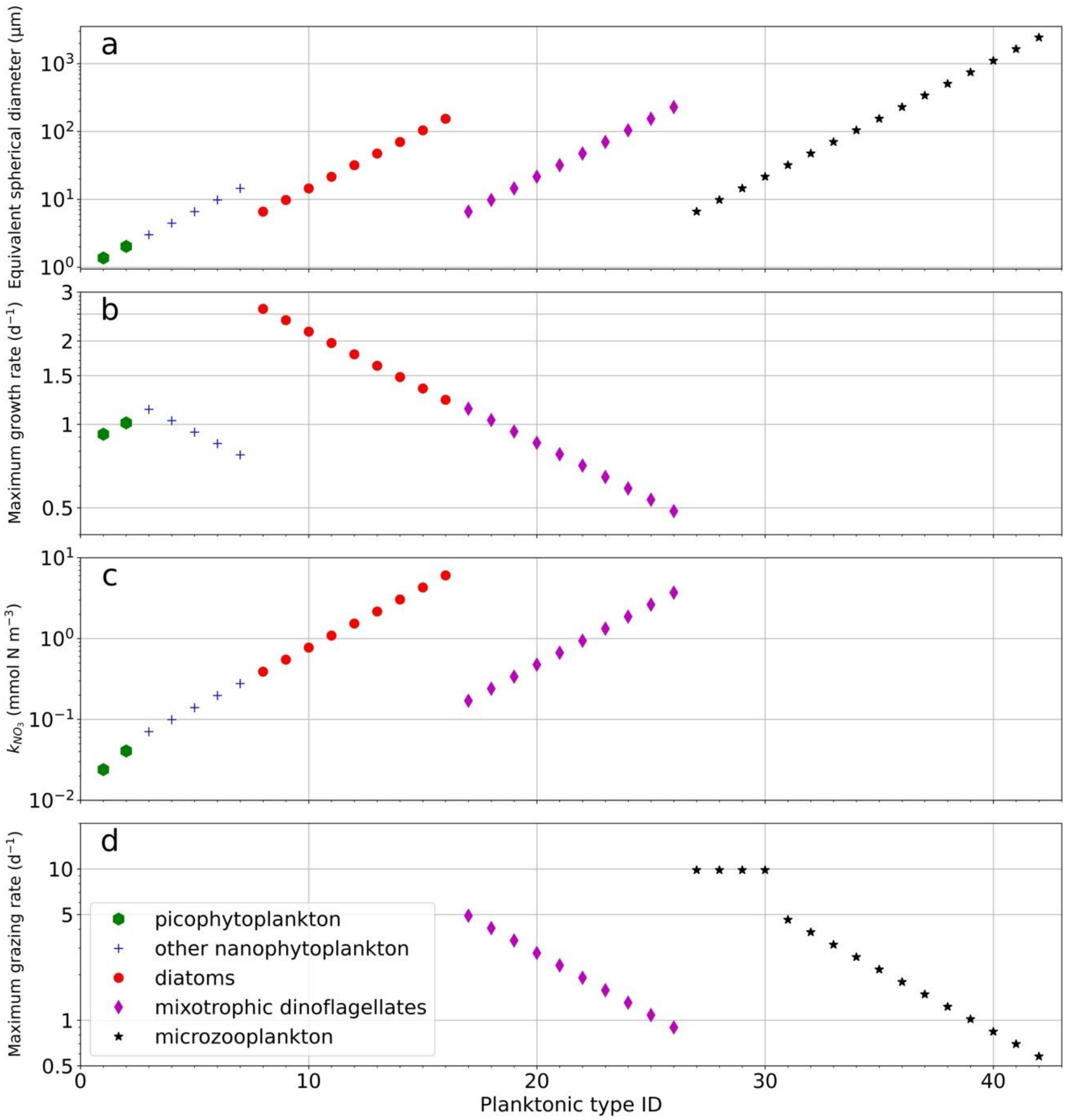

Figure 2. Parameters for each numerical type (each numerical species). a) Size (equivalent spherical diameter, ESD). b) Maximum growth rate (P^{C}_{max}). c) Half saturation for growth on nitrate (k_{NO_3}). d) Maximum grazing rate (g_{max}).

2.2.2 Configuring the reference simulation

The initial conditions of nitrate, silicic acid and phosphate were prescribed from in situ observations in 2015 and 2016 (Massicotte et al., 2020). Data could be averaged between mid-April and end of May in the two years (Figure 3a and Data S2 in Benoît-Gagné et al., 2024) because the observed nutrients were constant during this time (Figures 4c and S2a, b and c for 2016; not shown for 2015) and the stable sea ice conditions were likely responsible for this stability in the nutrient profiles during winter. There is no advection in a 1-D model, which prevents the supply of nutrients to the surface layer of the water column and results in their depletion. Compensation for the non-existing lateral advection and the absence of nutrient inputs by river runoff in the model was then necessary. The solution selected was the relaxation (reinitialization) of simulated nitrate, silicic acid and phosphate concentrations from January 1 to May 15 to in situ observations from mid-April to the end of May, during the ice-covered period at the ice camp. A relaxation coefficient of 1/30 d^{-1} was used. No relaxation occurs after May 15, 20 days before the start of snow melt and biological activity in the water column, according to the in situ ice camp data (Oziel et al., 2019, their Figure 10). A sensitivity experiment on the level of winter nitrate is presented in Section 3.6.

Model output from a 10-year spin-up period was used to provide initial conditions of ammonia, nitrite, total iron and dissolved organic and particulate organic matter. The same initial spin-up model results provided the total phytoplankton biomass (mmol C m^{-3}). This initial spin-up biomass was then divided equally between the 26 numerical phytoplankton types to be used as initial conditions for the reference simulation. The spin-up model output also provided the total zooplankton biomass which, again, was divided equally between the 16 numerical zooplankton types for initial conditions. At initialization, Chl *a* is acclimated to light, temperature and nutrients following Geider et al. (1998). But Chl *a* and the Chl:C ratio are calculated dynamically at each time step of the model.

The model time step was 1 h. The "reference" simulation was run forward for another 10 years with repeating forcing fields. Model results shown are from the last year of simulation. The phytoplankton established a regular pattern after 2 years, such that we can assume a "quasi-steady state" by year 10, at which time the initial conditions were no longer influencing the simulation results.

Before the sea ice break-up on July 18, the observed downwelling plane PAR just below sea ice in photon density flux, $E_{d,i}(z = 0^-, PAR[Q])$, was converted to the scalar PAR just below sea ice in photon density flux, $E_{0,i}(z = 0^-, PAR[Q])$, as described in Appendix A2.1. Observations from the Qikiqtarjuaq ice camp (Matthes et al., 2019) were used to estimate the conversion factors. After the sea ice break-up, the downwelling shortwave radiation just above surface in energy units, $E_s(z = 0^+, SW)$, from Smith et al. (2014) was transformed into the scalar PAR just below open water in photon density flux, $E_{0,w}(z = 0^-, PAR[Q])$, as described in Appendix A2.2. $E_{0,i}(z = 0^-, PAR[Q])$ and $E_{0,w}(z = 0^-, PAR[Q])$ were used as forcing fields (Data S5 in Benoît-Gagné et al., 2024). The scalar PAR at each depth (E_0) was calculated from $E_{0,i}(z = 0^-, PAR[Q])$ before the sea ice break-up and from $E_{0,w}(z = 0^-, PAR[Q])$ after the sea ice break-up as described in Appendix A2.3.

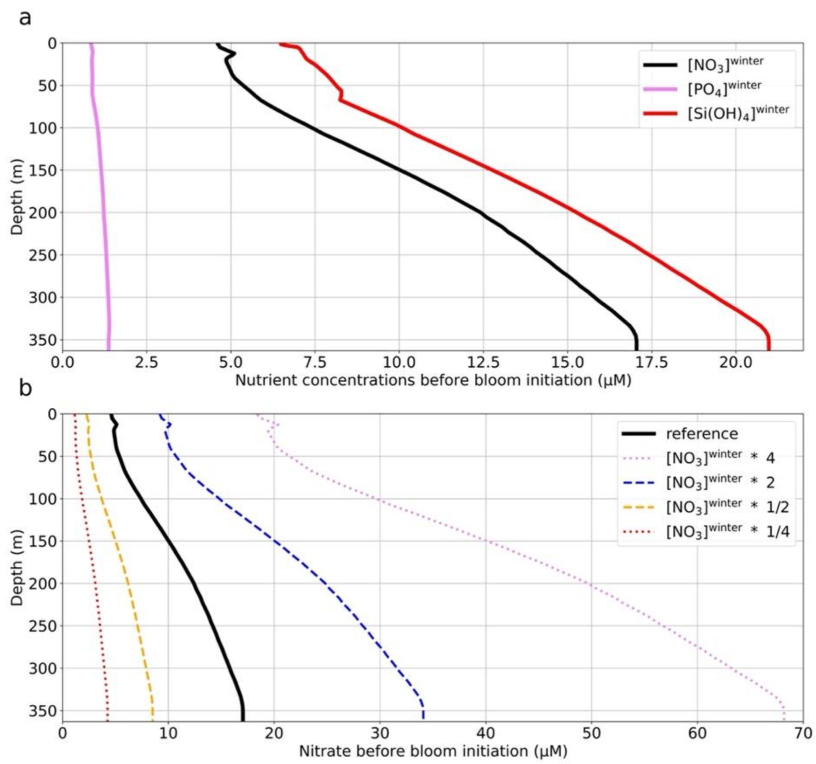

Figure 3. Nutrient concentrations between January 1 and May 15. The solid lines are the in situ nutrient concentrations at the Qikiqtarjuaq sea ice camps averaged between mid-April and end of May in 2015 and 2016. They are also the nutrient concentrations between January 1 and May 15 for the reference simulation (EXP-0). a) Nitrate ($[NO_3]^{winter}$, black), silicic acid ($[Si(OH)_4]^{winter}$, red) and phosphate ($[PO_4]^{winter}$, purple) concentrations between January 1 and May 15. b) Nitrate concentration ($[NO_3]^{winter}$, black) between January 1 and May 15. The dotted and dashed lines are the nitrate concentrations between January 1 and May 15 for the sensitivity simulations EXP-3 (Table 1). Note the different x-axis scales between panels a) and b).

2.2.3 Simulations

Model evaluation was performed by comparing the results of a reference simulation (EXP-0, Table 1; Data S6 in Benoît-Gagné et al., 2024) with in situ observations from the ice camp. We explored the tenth year of the reference simulation by segmenting it into: pre-bloom, bloom initiation and growth phase, and bloom peak. The day of the bloom initiation is defined as the last day of a 7-day positive accumulation period (following Boss and Behrenfeld, 2010). The bloom peak is defined as the day of maximum Chl *a*. We conducted a series of sensitivity experiments (Table 1) to explore the controls of the bloom timing: the magnitude of the biomass before the bloom initiation (EXP-1), treatment of light under sea ice (EXP-2) and nitrate concentration before the bloom initiation (EXP-3).

Table 1. Table of sensitivity experiments[a]

Variable	EXP-0	EXP-1	EXP-2	EXP-3
Minimum biomass	10^{-2}	$0, 10^{-3}, 10^{-1}, 10^{0}$	10^{-2}	10^{-2}
Light under sea ice	Light under snow and ice	Light under snow and ice	Opaque under snow, opaque under snow and ice	Light under snow and ice
Winter nitrate	Same	Same	Same	Differing

[a]The units of the minimum biomass are mmol C m^{-3} for each phytoplankton type.

3 Results

3.1 Ice camp observations

This section describes the observations measured at the ice camp and presented with dots on Figures 4 and 5. At the sea ice camp, snow melt occurred during the first half of June (Figure 4a and Oziel et al., 2019). Sea ice became thinner and melt ponds were created from the middle of June until the full sea ice break-up on July 18. The sea ice break-up necessarily led to the end of the ice camp campaign. The increase in the underwater light field in June and July (Figure 4b) corresponded to a decrease in the observed nutrient concentrations (Figure 4c) and an increase in vertically integrated phytoplankton biomass ($\sum C_{phyto}$, 0–100 m; Figure 4d) and chlorophyll *a* (∑Chl *a*, 0–100 m; Figure 4e).

The early peak of accumulation rate of ∑Chl *a* on May 9 was likely due to the flushing of sea ice algae from the melting ice. Hence, we considered the date of bloom initiation as May 27 (Figure S3 and Table S2), a date similar to the date calculated in Oziel et al. (2019). After the snow had melted during the first half of June, $\sum C_{phyto}$ and ∑Chl *a* increased significantly in mid-June causing a drawdown in nutrients. The highest ∑Chl *a* observed was on July 15, right before the sea ice cover disappeared at the ice camp. Although ∑Chl *a* may have reached a value higher than that of July 15 after the end of the ice camp campaign, for the purposes of this study we assume July 15 as the "peak" of the bloom. From the underwater light field, the depth of a "reference isolume" at 0.415 mol photons m^{-2} d^{-1} ($z_{0.415}$) was calculated (Letelier et al., 2004; Boss and Behrenfeld, 2010; Oziel et al., 2019). The significant increase in ∑Chl *a* in mid-June was correlated to the shoaling of this reference isolume (Figure 4e and f). This isolume followed the observed equivalent mixed layer depth (h_{BD}, as in Randelhoff et al., 2017; Figure 4f).

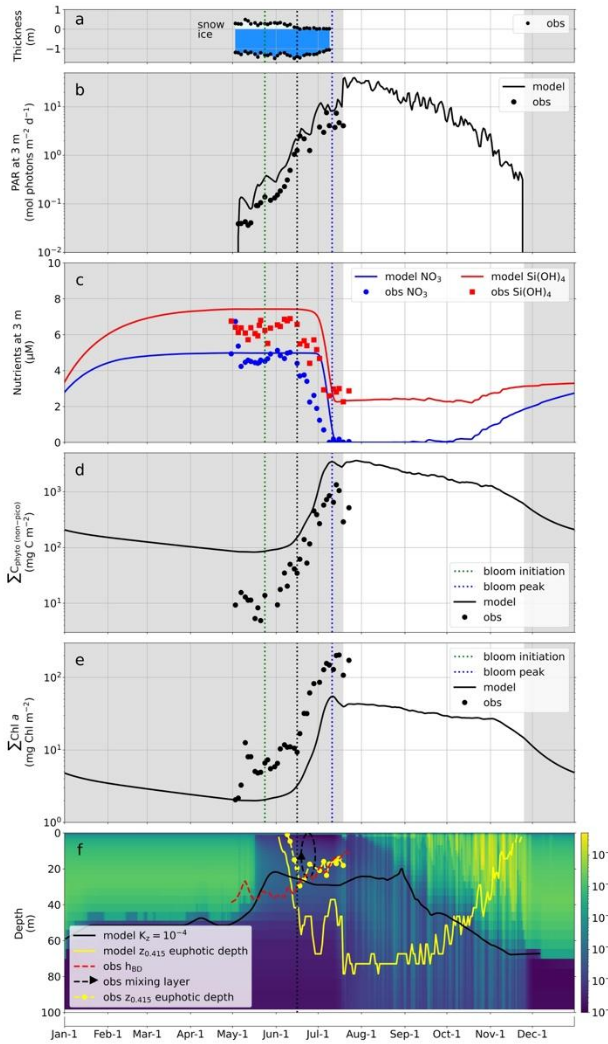

Figure 4. **Model output and observations for total phytoplankton.** a) Observed snow and ice thickness. b) Surface daily photosynthetically active radiation (PAR) at 3 m. Black dots are in situ daily downwelling plane PAR. Solid black line is the model daily scalar PAR from the MIT General Circulation Model *(*MITgcm). c) Surface nitrate concentration and silicic acid concentration at 3 m. Dots are in situ nutrient concentrations. Lines are the modelled nutrient concentrations from MITgcm. d) Vertically integrated biomass of phytoplankton (0–100 m). Dots are in situ biomass. The line is the model biomass from MITgcm. Note that picophytoplankton is not included in the analysis of the integrated biomass as this group was not part of the observations. e) Vertically integrated Chl *a* (0–100 m). Dots are in situ Chl *a*. The line is the model Chl *a* from MITgcm. f) Physical variables. The background is the model vertical turbulent diffusivity (K_z) from NEMO-LIM3. The depth at which model $K_z = 10^{-4}$ m^2 s^{-1} is the black solid line. The depth of the model reference isolume at 0.415 mol photons m^{-2} d^{-1} ($z_{0.415}$) from MITgcm is the yellow complete line. The depths of the observed equivalent mixed layer (h_{BD} as in Randelhoff et al., 2017) is the red dashed line. The depth of the observed mixing layer measured on June 23, 2016, as described in Oziel et al. (2019), is the black dashed arrow. The depth of the observed reference isolume at 0.415 mol photons m^{-2} d^{-1} ($z_{0.415}$) is the yellow dashed line. The vertical green, black and blue dotted lines are the dates of the simulated bloom initiation, the snow melt completion and the

simulated bloom peak, respectively. The grey shading represents the time of year before the sea ice break-up and after the sea ice freeze-up.

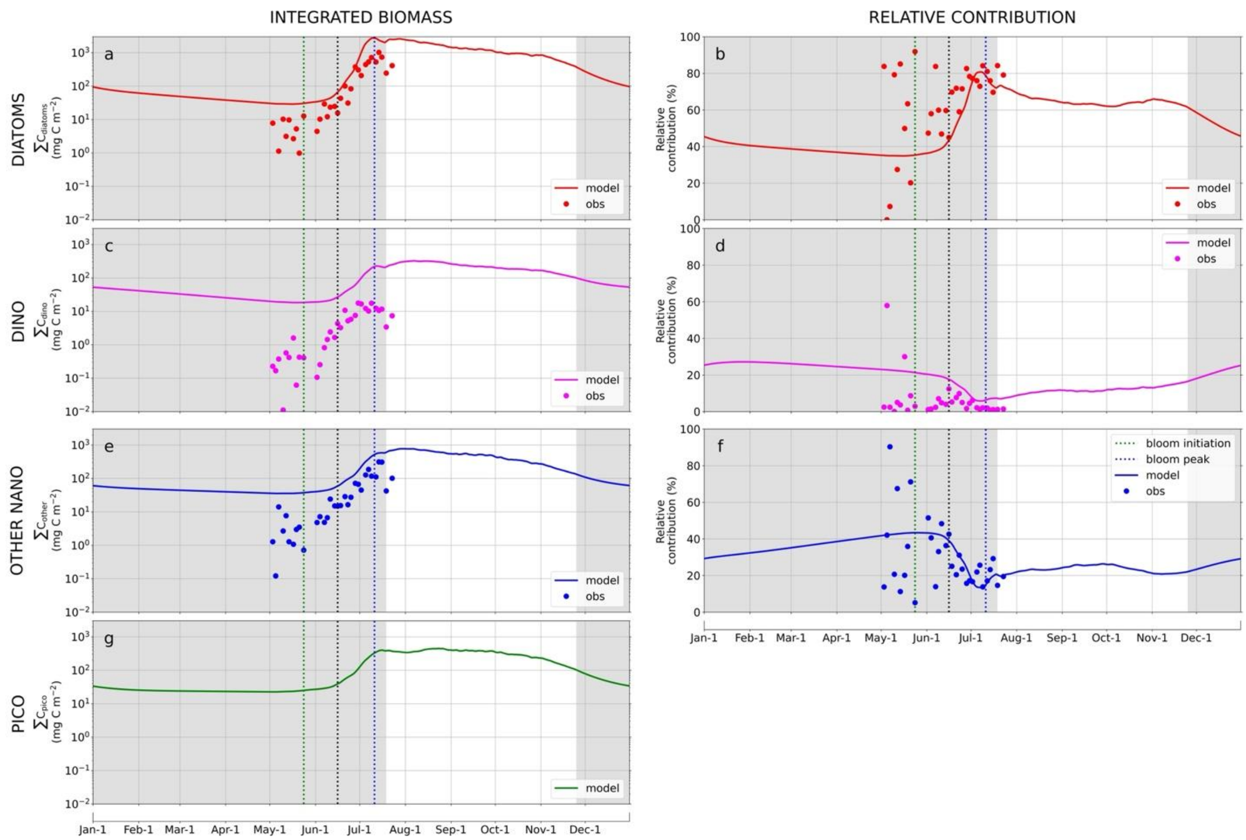

Figure 5. **Model output and observations by phytoplankton group.** Vertically integrated biomass of each functional group (0–100 m, left). Relative contribution of each functional group to the total (diatoms+dinoflagellates+other nanophytoplankton) biomass (right). a) Integrated biomass of diatoms. b) Relative contribution of diatoms. c) Integrated biomass of dinoflagellates. d) Relative contribution of dinoflagellates. e) Integrated biomass of other nanophytoplankton. f) Relative contribution of other nanophytoplankton. g) Integrated biomass of picophytoplankton. Picophytoplankton carbon biomass was not measured during the ice camp, as the Imaging FlowCytobot is not capable of imaging these smaller cells. The vertical green, black and blue dotted lines are the dates of the simulated bloom initiation, the snow melt completion and the simulated bloom peak, respectively. The grey shading represents the time of year before the sea ice break-up and after the sea ice freeze-up.

3.2 Reference simulation

The model was evaluated by comparing the simulated variables with observations. A Taylor diagram for the observational time series summarises the resulting statistics (Figure 6). The correlation coefficient (angular position) and normalised standard deviation (radial position) are performed on log-normalised fields. The correlation coefficient of the nutrient concentrations was greater than 0.7 for each nutrient. Observed ∑Chl *a* was particularly well captured by the model with a correlation coefficient of 0.89. ∑Chl *a* variability was also well captured with a normalised standard deviation of 1.05. The model captures the diatoms and other nanophytoplankton biomass well (correlation coefficients of 0.82 and 0.75, respectively), and slightly worse for the dinoflagellates (correlation coefficient of 0.63). We discuss the time series of the reference simulation further in terms of three phases: pre-bloom (before May 23), bloom initiation and growth, and bloom peak on July 10.

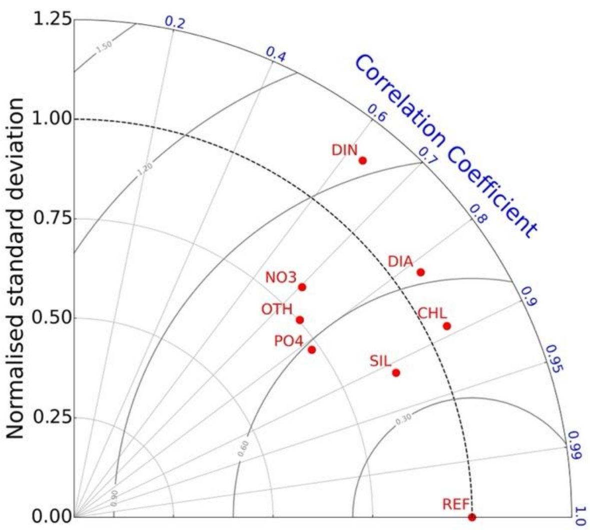

Figure 6. Taylor diagram. Taylor diagram evaluating the model with the observations at the Qikiqtarjuaq ice camp in 2016. The angular position indicates the correlation coefficient between model and observed values. The radial position is their normalised (by observed standard deviation) standard deviation. Statistics are performed on log-normalised fields. CHL indicates Chl *a* concentration obtained by high-performance liquid chromatography; DIA, diatoms; DIN, dinoflagellates; NO3, nitrate; OTH, other nanophytoplankton; PO4, phosphate; SIL, silicic acid; REF, perfect match between model and observations.

3.2.1 Pre-bloom period

This section describes the observed and simulated quantities before the simulated bloom initiation represented by the vertical green dotted line on May 23 in Figures 4 and 5. In both model and observations, snow melt had not yet started (Figure 4a) and simulated underwater PAR was low (Figure 4b). Simulated surface nutrient concentrations were high (Figure 4c), matching observations. Simulated integrated biomass (0–100 m, $\sum C_{phyto}$) and simulated integrated Chl *a* (0–100 m, ∑Chl *a*) were low (Figure 4d and e, respectively). The simulated biomass was higher than observed, though the simulated Chl *a* (2 mg Chl m^{-2}) was on the lower bound of the observed values of Chl *a* (2–23 mg Chl m^{-2}).

3.2.2 Bloom initiation and growth period

The bloom initiation occurred on May 23 in the reference simulation, 4 days before the observations (Figure 4e). A steep increase in the underwater PAR between bloom initiation and the complete melt of the snow cover on June 15 (Figure 4b) caused a slow growth period of both observed and simulated $\sum C_{phyto}$ and ∑Chl *a* (Figure 4d and e, respectively). This increase in biomass was not enough to decrease the nutrient concentrations significantly. In both model and observations, the depth of the reference isolume increased (Figure 4f).

The disappearance of the snow cover on June 15 (black dotted vertical line on panels a and b of Figure 4) allowed the underwater PAR to increase enough to cause a fast growth period (Figure 4a and b). This fast growth period is visible in both observed and simulated $\sum C_{phyto}$ and ∑Chl *a* between the complete melt of the snow cover on June 15 and the simulated bloom peak on July 10 (blue dotted vertical line on panels d and e of Figure 4). Simulated and observed nitrate was depleted at the end of this fast growth period, but not silicic acid (Figure 4c). During the fast growth period, the reference isolume was deeper than observed (Figure 4f). We discuss this discrepancy in Section 3.2.3.

The simulated biomass of the diatoms increased at the same time as the observations, though the model overestimated the biomass at the start and end of the growth period (Figure 5a). Similarly, the simulated biomass of the other nanophytoplankton increased at the same time as the observations, though the biomass was too high over the full season (Figure 5e). The model captured the relative contributions (%) of diatoms and other nanophytoplankton (Figure 5b and f, respectively) during this period. In particular, the fast growth period between the disappearance of the snow cover and the bloom peak was associated with a change in the phytoplankton assemblage from other nanophytoplankton dominance to diatoms.

3.2.3 Bloom peak

The depletion of simulated surface nitrate inhibited the growth of phytoplankton after July 10. The steep increase in surface PAR associated with the sea ice break-up of July 18 led to photoacclimation of the numerical phytoplankton. This decrease in the Chl:C ratio after the sea ice break-up caused a decoupling between $\sum C_{phyto}$ and ∑Chl *a*. The ∑Chl *a* peak occurred on July 10, 5 days before the observations. $\sum C_{phyto}$ from the IFCB continued to increase reaching a maximum on July 27 due to the decoupling. Following previous studies of the Qikiqtarjuaq sea ice camp (Oziel et al., 2019; Massicotte et al., 2020), maximum ∑Chl *a* rather than maximum $\sum C_{phyto}$ was defined as the bloom peak.

The simulated maximum magnitude of ∑Chl *a* of 55 mg Chl m^{-2} was underestimated relative to the observations of 204 mg Chl m^{-2}. The fact that the simulated $\sum C_{phyto}$ was equal to or above the observations (Figure 4d) but that the simulated ∑Chl *a* was below the observations (Figure 4e) was indicative of an underestimation of the Chl:C ratio. This underestimated Chl *a* also led to light penetrating too deep in the simulation (Figure 4f). The trend of the simulated mixed layer depth ($K_z = 10^{-4}$ m^2 s^{-1}) differed from the trend of the observed equivalent mixed layer depth (h_{BD}, as in Randelhoff et al., 2017) that was shoaling from 40 m to 10 m during this period of time. Despite underestimating the Chl *a* concentration, the temporal trends correlated well with the observations (Figures 4 and S2) and the subsurface chlorophyll maximum was captured (Figure S2). The biomass of the dinoflagellates was overestimated particularly after the bloom peak (Figure 5c).

3.3 The role of biomass before bloom initiation

We conducted a series of sensitivity experiments (Table 1) to explore controls of the bloom timing. In the model a minimum biomass threshold ($C_{min,j}$) was set below which a phytoplankton type experiences no losses such as grazing, maintenance or cell death to account for overwinter survival. In the reference simulation (EXP-0), $C_{min,j}$ was set to 10^{-2} mmol C m^{-3} for each phytoplankton type. This parameterization allowed the model to maintain winter Chl *a* like that observed at the ice camp (Figure 4e) and in other regions of the Arctic Ocean (see Section 4 for more discussion). In the first set of sensitivity experiments (EXP-1; Figures 7 and S4), this threshold was either increased ($C_{min,j} = 10^{0}$ and 10^{-1} mmol C m^{-3}) or decreased ($C_{min,j} = 10^{-3}$ mmol C m^{-3} and 0). A higher biomass before bloom initiation ($C_{min,j} = 10^{0}$ and 10^{-1} mmol C m^{-3}) caused an earlier bloom peak on July 2 (–8 days) and July 5 (–5 days), respectively. A lower biomass before the bloom initiation ($C_{min,j} = 10^{-3}$ mmol C m^{-3} and 0) delayed the bloom peak more substantially to July 16 (+6 days) and July 30 (+20 days), respectively.

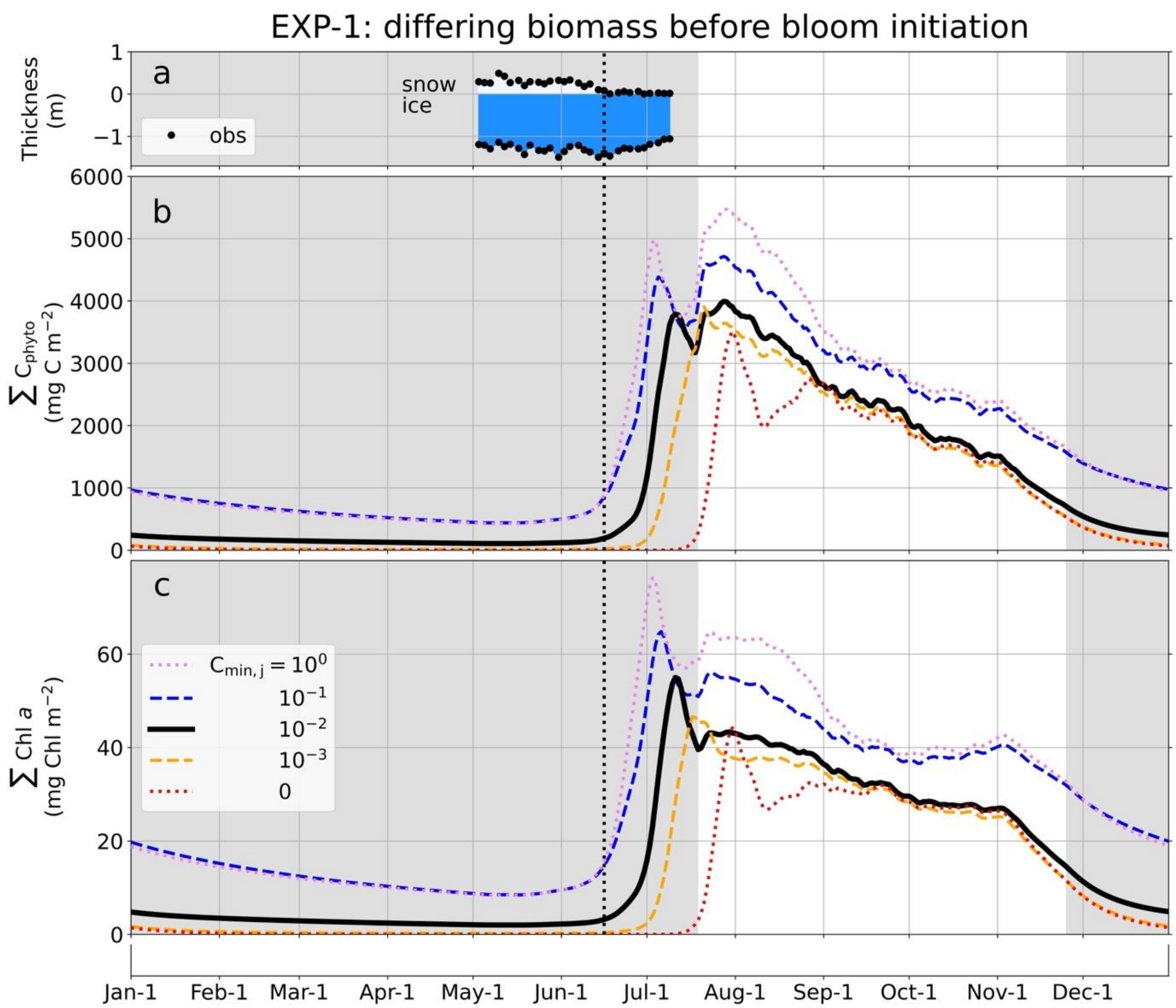

Figure 7. Sensitivity simulations for total phytoplankton: EXP-1 prescribed minimum biomass. The minimum biomass ($C_{min,j}$) was prescribed at 0, 10^{-3}, 10^{-2}, 10^{-1} and 10^{0} mmol C m^{-3} for each of the 26 numerical phytoplankton types. The minimum biomass for the reference simulation was 10^{-2} mmol C m^{-3}

(solid black line). This solid black line is the same output as shown in Figure 4d and e for the reference simulation. a) Observed snow and ice thickness. b) Vertically integrated biomass of phytoplankton (0–100 m). c) Vertically integrated Chl *a* (0–100 m). The vertical black dotted line is the date of the snow melt completion. The grey shading represents the time of year before the sea ice break-up and after the sea ice freeze-up.

3.4 The role of light under sea ice

In the second set of sensitivity experiments (EXP-2), we explored the importance of light in controlling bloom timing. In the reference simulation (EXP-0), the observed light just below sea ice, both for snow-covered sea ice and bare sea ice, was used as input for the model (Figures 8 and S5). In EXP-2.1, snow was considered opaque so that light just below snow-covered sea ice was set to 0 (Figure 8b). In EXP-2.2, both snow-covered sea ice and bare sea ice were considered opaque such that in this experiment there was no light below sea ice, both snow-covered sea ice and bare sea ice.

Removing light under snow-covered sea ice (EXP-2.1) delayed the bloom initiation to June 22 (+30 days) and the bloom peak to July 16 (+6 days; Figure 8c and d). Removing light under all sea ice (EXP-2.2) caused greater delays: in this case, the bloom initiation was delayed until July 25 (+63 days) and the bloom peak occurred only on August 7 (+28 days).

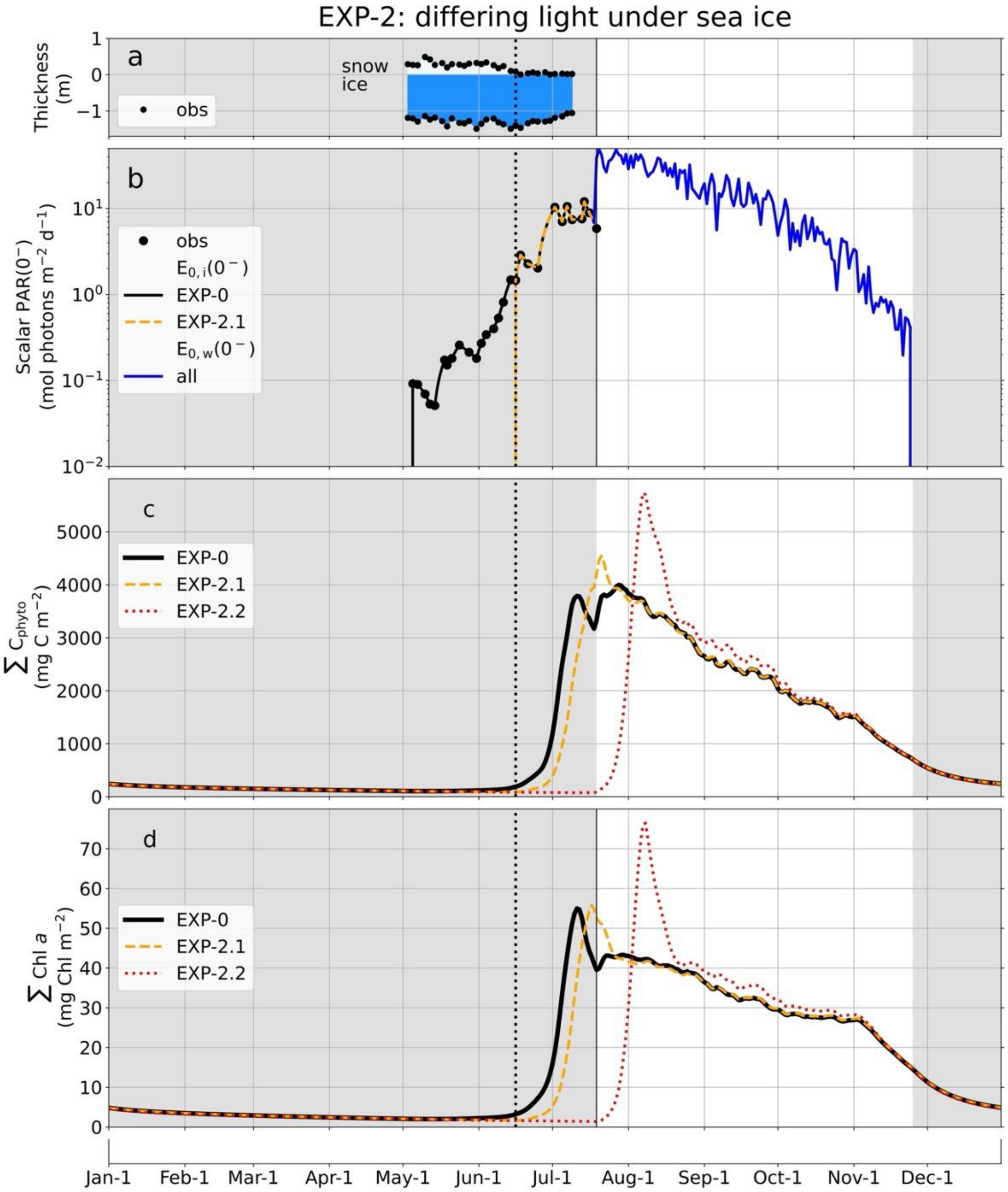

Figure 8. Sensitivity simulations for total phytoplankton: EXP-2 with differing light under sea ice. EXP-0 (reference simulation, solid black line) had light under snow-covered sea ice and under bare sea ice. EXP-2.1 (orange dashed line) had no light under snow-covered sea ice but had light under bare sea ice. EXP-2.2 (red dotted line) had no light under snow-covered sea ice and no light under bare sea ice; this line is not visible on panel b because its value was 0 and the y-axis is logarithmic. All the simulations had the same light under open water (solid blue line in panel b). a) Observed snow and ice thickness. b) Scalar photosynthetically active radiation (PAR) irradiance just below the surface given as input to the model, $E_0(0^-)$. The scalar PAR irradiance is just below sea ice, $E_{0,i}(0^-)$, until July 18 and just below open water, $E_{0,w}(0^-)$, after July 18. Black dots are observed in situ scalar PAR irradiance just below sea ice. c) Vertically integrated biomass of phytoplankton (0–100 m). d) Vertically integrated Chl *a* (0–100 m). The

vertical black dotted line is the date of snow melt completion. The grey shading represents the time of year before sea ice break-up (left) and after sea ice freeze-up (right).

3.5 The role of nitrate before bloom initiation

To explore the importance of the winter pool of nitrate on the timing of the bloom peak, a third set of sensitivity simulations considered different winter nitrate concentrations (EXP-3; Table 1). In the reference simulation EXP-0, the winter nutrients were relaxed to in situ observations at the Qikiqtarjuaq sea ice camps averaged between mid-April and end of May in 2015 and 2016 (Figure 3a). In the sensitivity simulations EXP-3 (Figures 9 and S6), the winter nitrate concentrations were instead relaxed to 1/4, 1/2, 2 and 4 times that in the reference simulation (Figure 3b).

Decreasing nitrate by a factor of 2 or 4 decreased the magnitude of the bloom peak from 55 mg Chl m^{-2} to 40 mg Chl m^{-2} and 27 mg Chl m^{-2}, respectively (Figure 9c). This decrease, in turn, caused a bloom peak slightly earlier on July 8 (–2 days) and July 6 (–4 days), respectively. The change in timing was much less than one would expect from the change in nutrients. Conversely, increasing nitrate before the bloom initiation by a factor of 2 or 4 increased marginally the magnitude of the bloom peak from 55 mg Chl m^{-2} to 59 mg Chl m^{-2} in both cases. Consequently, the bloom peak was barely delayed to July 11 (only +1 day).

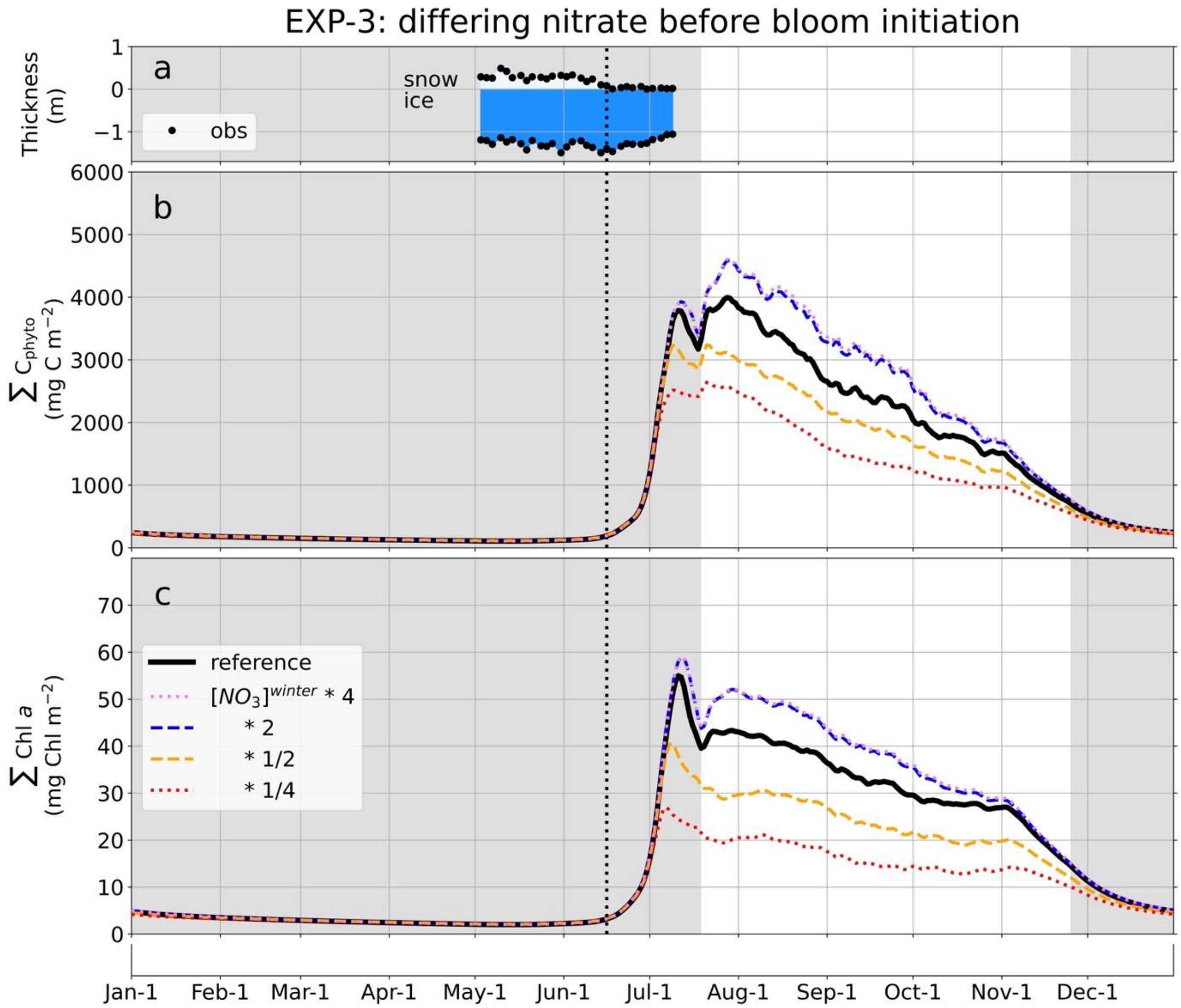

Figure 9. Sensitivity simulations for total phytoplankton: EXP-3 prescribed pre-bloom nitrate concentrations. Nitrate concentrations before the bloom initiation ($[NO_3]^{winter}$) were prescribed at 4, 2, 1/2 and 1/4 times that in the default simulation (solid black line). This solid black line is the same output as shown in Figure 4d and e for the reference simulation. a) Observed snow and ice thickness. b) Vertically integrated biomass of phytoplankton (0–100 m). c) Vertically integrated Chl *a* (0–100 m). The vertical black dotted line is the date of snow melt completion. The grey shading represents the time of year before sea ice break-up (left) and after sea ice freeze-up (right).

4 Discussion

Our study has shown that the overwintering biomass was an important control on the timing of the bloom peak (EXP-1; Figure 7). When the biomass before bloom initiation was lower than observed there was a delay in the peak Chl *a*. The simulated Chl *a* before the bloom initiation achieved with the $C_{min,j}$ of the reference simulation (EXP-0) was between 10^{-2} and 10^{-1} mg Chl m^{-3}, like the observed Chl *a* in May at the Qikiqtarjuaq ice camp (Figure S7). Randelhoff et al. (2020) measured Chl *a* with gliders in offshore Baffin Bay during the winters 2017–2018 and 2018–2019. Their values were also between 10^{-2} and 10^{-1}

mg Chl m^{-3} (their Figure 2e), supporting that a numerical winter Chl *a* above 10^{-2} mg Chl m^{-3} was realistic. The impact of pre-bloom biomass on the timing of the phytoplankton bloom peak is not surprising and has also been highlighted for ice algal growth and bloom timing (Mortenson et al., 2017; Haddon et al., 2024).

In our model, a value range of 10^{-2} to 10^{-1} mg Chl m^{-3} for Chl *a* before bloom initiation was achieved by halting any further losses from metabolism, grazing or other mortality (terms 2 and 3 in Equation 1) when the biomass of one type of phytoplankton dropped below $C_{min,j}$. This parameterization was necessary to maintain an overwintering biomass, but is obviously an extreme oversimplification of complex processes controlling the survival of phytoplankton communities during winter. The numerical $C_{min,j}$, however, could compensate for excessive phytoplankton sinking and dilution in the model and could also represent the missing three-dimensional features of the sea ice such as production in leads. This simple implementation of a threshold biomass is the minimum parameterization needed in a biogeochemical model to mimic the particular conditions of the Arctic. It might also apply to the Austral Ocean given polar night there as well. A similar parameterization has been implemented by several model studies (Mortenson et al., 2018; Christian et al., 2022; Bertin et al., 2023; Haddon et al., 2024), but none of the studies provided detailed documentation of the impacts. Chl *a* in the oligotrophic subtropical gyres falls between 10^{-2} and 10^{-1} mg Chl m^{-3} (Kuhn et al., 2023), similar to winter observations in Baffin Bay. These Chl *a* values suggest that carbon biomass is low and comparable in both systems. However, these two systems differ in the seasonality of the zooplankton predation, as the pressure of zooplankton grazing is continuous in oligotrophic tropical gyres. Therefore, using a parameterization that stops grazing in oligotrophic tropical gyres would not be appropriate, and $C_{min,j}$ should not be used globally. A simple workaround could be an empirical relationship between the latitude and the $C_{min,j}$ threshold, while a more comprehensive solution could be the decomposition of the linear mortality into various loss terms, each one mechanistically formulated (e.g., senescence, viral lysis of phytoplanktonic cells, etc.).

However, a clearer understanding of what maintains the overwintering biomass is needed for newer and better parameterizations. By implementing a realistic overwintering biomass and demonstrating its importance, this study is a first step in its mechanistic implementation. This implementation would benefit from the results of laboratory experiments at extremely low light. For example, the limitation for growth by light (γ^I) could be modified in winter to allow more phototrophy at low levels (Kvernvik et al., 2018; Hancke et al., 2018). The mortality term ($m_{p,j}$) could be reduced in winter to represent reduced metabolism (Lacour et al., 2019; Kennedy et al., 2020; Joli et al., 2024) and sparing consumption of storage lipids (Morin et al., 2020). In winter, mixotrophy (Vader et al., 2015; Błachowiak-Samołyk et al., 2015; Marquardt et al., 2016; Kvernvik et al., 2018; Stoecker and Lavrentyev, 2018; Johnsen et al., 2020) could be enhanced or osmotrophy (Wen et al., 2002; Lavoie et al., 2018; Johnsen et al., 2020) could be activated. Winter grazing by zooplankton could be reduced by modifying the limitation of grazing by temperature (γ^T) in winter to represent the negligible losses to herbivorous grazing (Frost, 1993; Rose and Caron, 2007) or by implementing diapause on mesozooplankton (Baumgartner and Tarrant, 2017). Another strategy of survival during the polar night is resting stage formation (Johnsen et al., 2020).

Several studies have reported that Arctic diatoms can survive in the dark for months and start photosynthesis rapidly (within a few hours) when light returns (e.g., Lacour et al., 2019; Kennedy et al., 2020; Morin et al., 2020; Handy et al., 2024): a finding that has been confirmed in situ in Svalbard (Kvernvik et al., 2018). Both field experiments and laboratory experiments suggest that photosynthesis can occur at very low light from 0.17 to 1 µmol photons m^{-2} s^{-1} (Geider et al., 1986; Hancke et al., 2018; Kvernvik et al., 2018). Accumulation of biomass generally does not occur until higher light levels between 1.2 and 2.3 µmol photons m^{-2} s^{-1} are available (Geider et al., 1986; Ardyna et al., 2020b). However, biomass accumulation has been observed to occur at levels lower than previously thought, for example, in February in offshore Baffin Bay shortly after the winter solstice (Randelhoff et al., 2020). Recent field observations (Ardyna et al., 2020b; Randelhoff et al., 2020) show that even in Arctic marine ecosystems, blooms can start before stratification occurs, which is coherent with the dilution recoupling hypothesis (Behrenfeld, 2010; Behrenfeld and Boss, 2018). Importantly, the minimum light thresholds for photosynthesis and a positive accumulation rate remain uncertain. Further laboratory experiments with extremely low irradiations are needed.

The importance of under-ice PAR in triggering the initiation of the under-ice bloom is better understood (Ardyna et al., 2020a; 2020b). With the absence of light under snow-covered sea ice (EXP-2.1) and the absence of light under any sea ice (EXP-2.2), the bloom peak was delayed significantly (+6 and +28 days, respectively).

Finally, the magnitude of the bloom peak was only slightly affected by the winter pool of nitrate (EXP-3, Figure 9). Nitrate concentration before the bloom initiation had no effect on the initiation of the bloom and was only a modest control on the timing of the bloom peak. Because the accumulation of phytoplankton was exponential, a linear variation in winter nitrate and thus the magnitude of the bloom at its peak did not change the date of the bloom peak by much.

The model used in this study did not include a sympagic component. Previous modelling studies have shown some influence of ice algal production on the magnitude of the phytoplankton bloom in Arctic marine ecosystems (Hayashida et al., 2017; Mortenson et al., 2017). These studies suggested that seeding of phytoplankton production by ice algae sloughing from the sea ice in spring influenced the timing of both the bloom initiation and bloom peak by a few days. However, a review of in situ studies showed that only when extreme meteorological events trigger mass release of ice algae into the water column is seeding from sea ice an important control of the timing of under-ice blooms (Ardyna et al., 2020a). Another observation that may be interpreted as against seeding by ice algal sloughing is that the genera of polar diatoms observed in the winter water column (Vader et al., 2015; Kvernvik et al., 2018) are also those found in the spring phytoplankton bloom (Hoppe, 2022). Another impact of sea ice algae on phytoplankton production involves a shading effect. In simulations, ice algal shading can have a strong impact on the timing of the phytoplankton bloom under the ice when ice algal biomass is high (Castellani et al., 2017; Hayashida et al., 2019). In this study, observed PAR just below the (real) sea ice, and thus including the shading impact of sea ice algae, was used as a forcing field. Further research on the impact of sea-ice algae is warranted but is beyond the scope of this study.

The physical variables at the location of the ice camp were close to the conditions of offshore western Baffin Bay (Appendix 6.4). The conditions at the ice camp followed the dynamics described for offshore areas with phytoplankton bloom initiation occurring while there was still ice (Randelhoff et al., 2019; 2020). The processes at the ice camp and in western Baffin Bay (of which the ice camp is representative) are typical of an outflow shelf environment. Seasonal sea ice cover fosters sizable pelagic blooms as soon as sea ice becomes translucent due to the deepening of the euphotic zone and the shoaling of the mixed layer depth (Randelhoff et al., 2019) in a manner similar to other outflow shelf environments of the Arctic

Ocean, such as the Canadian Arctic Archipelago and the East Greenland shelf (Ardyna et al., 2020a). These outflow shelves are expected to react similarly to climate change (Ardyna and Arrigo, 2020). Thus, we believe that our study has broader implications than the single location studied here, although our study is specific to the polar regions.

5 Conclusion

Our study has shown that phytoplankton biomass at the end of winter is a key parameter for accurately modelling the spring phytoplankton bloom in a seasonal sea ice zone. Though a minimum threshold biomass parameterization has been used in previous studies, to our knowledge this study provides the first published sensitivity analysis. Our study also agrees with earlier results about the necessity of a reasonable representation of light transmittance through sea ice, especially for bare sea ice compared to snow-covered sea ice. Here we have shown that winter biomass and light under sea ice are comparably important controls for the timing of the bloom peak (+20 days when no winter biomass and +28 days when no light under sea ice). Research campaigns so far have generally concentrated efforts on measuring light in the water and have not focused on measuring winter biomass. Our results have shown that both observations will be important for further understanding of the spring phytoplankton bloom. This study highlights the need for field and laboratory experiments to gain a more precise understanding on the acclimation and adaptations by phytoplankton to maintain a balance between biomass growth and losses during the harsh Arctic winter. A better characterization of the underwater light field during the polar night will also be worthwhile, as darkness is never complete because of moonlight among other reasons (Cohen et al., 2020). Only with a better understanding of the mechanisms of survival of phytoplankton during winter we will be able to parameterize this aspect more realistically in models. Better models of Arctic ecosystems are urgently needed as this region has warmed four times faster than the global average since 1979, a phenomenon known as Arctic amplification (Rantanen et al., 2022). The crude parameterization of a minimum phytoplankton biomass threshold is, however, an initial step towards more accurately representing the timing of the bloom peak.

6 Appendix

6.1 A1 Biogeochemical/ecosystem model

Only an overview of the model is presented here. More detail and equations can be found in Dutkiewicz et al. (2015; 2020) and at https://darwin3.readthedocs.io/en/latest/phys_pkgs/darwin.html (accessed May 30, 2024). See Tables S3, S4 and S5 for the units of the variables, the values of the constants and the coefficients for allometric scaling, respectively.

6.1.1 A1.1 Phytoplankton growth

The carbon-specific photosynthesis rate of phytoplankton (P^C) is dependent on maximum growth rate ($P^C{}_{max}$; Figure 2b) and limitation for growth by nutrients, temperature and light (γ^R, γ^T, γ^I, respectively, between 0 and 1) such that

2. $P^C = P^C_{max}\gamma^R\gamma^T\gamma^I$.

A limitation for growth of 0 means no growth because there are no nutrients, for example, or no light. A limitation for growth of 1 means no limitation for growth. The limitation for growth by nutrients, temperature and light is described in Appendices A1.2, A1.3 and A1.4, respectively.

6.1.2 A1.2 Nutrient limitation for growth

The half saturation for growth on nitrate (k_{NO_3}; Figure 2c) is modelled as in Dutkiewicz et al. (2020) using the model Monod formulation of growth rate (Follows et al., 2018):

3. $k_{NO_3} = K_{NO_3}\frac{P^C_{max}Q^{min}_N}{V^{max}_{NO_3}}$.

The cell nutrient uptake half saturation constant on nitrate (K_{NO_3}; Figure S8a) is dependent on size but not on group as

4. $K_{NO_3} = a_{K_{NO_3}}V^{b_{K_{NO_3}}}$,

where $a_{K_{NO_3}}$ and $b_{K_{NO_3}}$ are coefficients for allometric scaling and V is the cell volume. The maximum growth rate ($P^C{}_{max}$; Figure 2b) is dependent both on size V and on group g as

5. $P^C_{max} = a_{P^C_{max},g}V^{b_{P^C_{max},g}}$,

where $a_{P^C_{max},g}$ and $b_{P^C_{max},g}$ are the coefficients for allometric scaling dependent on group g. The cell minimum stoichiometric quota of nitrogen relative to carbon (Q^{min}_N; Figure S8b) is dependent on size but not on group as

6. $Q^{min}_N = a_{Q^{min}_N}V^{b_{Q^{min}_N}}$,

where $a_{Q^{min}_N}$ and $b_{Q^{min}_N}$ are coefficients for allometric scaling. The cell nutrient uptake rate of nitrate relative to carbon ($V^{max}_{NO_3}$; Figure S8c) is dependent on size but not on group as

7. $V_{NO_3}^{max} = a_{V_{NO_3}^{max}} V^{b_{V_{NO_3}^{max}}}$,

where $a_{V_{NO_3}^{max}}$ and $b_{V_{NO_3}^{max}}$ are coefficients for allometric scaling. The cell elemental C:N:Si:P:Fe stoichiometry is 120:16:16:1:0.001. (Only diatoms have silicon.) The half saturation for growth on silicic acid ($k_{Si(OH)_4}$) is computed using this stoichiometry as

8. $k_{Si(OH)_4} = k_{NO_3} \times \frac{16}{16} = k_{NO_3}$.

The half saturation for growth on phosphate (k_{PO_4}) is computed similarly as

9. k_{PO_4}=$k_{NO_3} \times \frac{1}{16}$.

The half saturation for growth on iron (k_{Fe}) is computed similarly as

10. k_{Fe}=$k_{NO_3} \times \frac{1}{16000}$.

The half saturation for growth on ammonia (k_{NH_4}) is computed with a factor of 1/2 because phytoplankton preferentially use ammonia:

11. k_{NH_4}=$k_{NO_3} \times \frac{1}{2}$.

The most limiting nutrient determines the value of the nutrient limitation for growth (γ^R, between 0 and 1) as

12. $\gamma^R = min\left(\frac{R_{NO_3}+R_{NO_2}}{R_{NO_3}+R_{NO_2}+k_{NO_3}} e^{-\sigma_{NH_4} R_{NH_4}} + \frac{R_{NH_4}}{R_{NH_4}+k_{NH_4}}, \frac{R_{Si(OH)_4}}{R_{Si(OH)_4}+k_{Si(OH)_4}}, \frac{R_{PO_4}}{R_{PO_4}+k_{PO_4}}, \frac{R_{Fe}}{R_{Fe}+k_{Fe}}\right)$,

where σ_{NH_4} is the coefficient for ammonia inhibition of nitrogen uptake and R_{NO_3}, R_{NO_2}, R_{NH_4}, $R_{Si(OH)_4}$, R_{PO_4} and R_{Fe} are the concentrations of nitrate, nitrite, ammonia, silicic acid, phosphate and iron, respectively.

6.1.3 A1.3 Temperature limitation for growth

Temperature modulation for growth (γ^T, between 0 and 1) is calculated from the ambient temperature (T) as in Dutkiewicz et al. (2015):

13. $\gamma^T = \tau_T exp\left(A_T\left(\frac{1}{T} - \frac{1}{T_N}\right)\right)$,

where τ_T is a normalisation factor for temperature function, A_T is a constant and T_N is the reference temperature. The interval of ambient temperature in the forcing fields of the simulation was –1.8°C to 2.9°C. Following Equation 13, the interval of modification of growth rate by temperature was 0.27 to 0.34. The term γ^T was the same for all plankton types.

6.1.4 A1.4 Light limitation for growth

Light limitation for growth (γ^I, between 0 and 1) follows Geider et al. (1998) as described in Dutkiewicz et al. (2015):

14. $\gamma^I = 1 - exp\left(\frac{-\alpha^{chl} E_0 \theta}{P_{max}^C \gamma^R \gamma^T} \frac{1}{M_C} \frac{24h}{d}\right)$,

where α^{chl} is a constant linear initial slope of the Chl *a*-specific photosynthesis versus irradiance curve in nutrient-replete conditions (Figure S1b), E_0 is the scalar PAR, θ is the Chl:C ratio, $P^C{}_{max}$ is the maximum growth rate (Figure 2b), γ^R is the nutrient limitation for growth, γ^T is the temperature modulation for growth and M_C is the molar mass of carbon. The last two factors of Equation 14 are required to correctly convert the units of θ and α^{chl}. The production of new Chl *a* follows Geider et al. (1997) and Geider et al. (1998) as described in Dutkiewicz et al. (2015).

6.1.5 A1.5 Grazing

Grazing follows from Dutkiewicz et al. (2020) as

15. $g_{jk} = g_{max,k} \gamma^T \frac{\sigma_{jk} B_j}{G_k} \frac{G_k^2}{G_k^2 + k_p^2}$.

The subscript *j* is the prey, and the subscript *k* is the predator. The term g_{jk} is the grazing rate. The maximum grazing rates ($g_{max,k}$; Figure 2d) are from observations (Jeong et al., 2010; Taniguchi et al., 2014). The term σ_{jk} is palatability, B_j is prey biomass and G_k is the palatability-weighted total phytoplankton biomass as

16. $G_k = \sum_j \sigma_{jk} B_j$.

The grazing half saturation rate (k_p) is a constant.

6.2 A2. Scalar photosynthetically active radiation

In this section, we provide a description of the calculation of the scalar PAR at each depth. Appendix A2.1 describes the calculation of the scalar PAR just below the surface when the surface was sea ice before July 18. Appendix A2.2 describes the calculation of the scalar PAR just below the surface when the surface was open water from July 18. Appendix A2.3 describes the calculation of the scalar PAR at each depth from the scalar PAR just below the surface. Equations from Appendix A2.3 were used the whole year. See Tables S6 and S7 for the units of the variables and the values of the constants, respectively.

6.2.1 A2.1 Scalar photosynthetically active radiation below sea ice

The downwelling plane PAR just below sea ice in photon density flux, $E_{d,i}(z = 0^-, PAR[Q])$ (Data S5 in Benoît-Gagné et al., 2024), was measured as described in Oziel et al. (2019) and Massicotte et al. (2020). The average cosine (μ_d) was used to calculate the downwelling scalar PAR just below sea ice in photon density flux, $E_{0d,i}(z = 0^-, PAR[Q])$:

$$17.\ E_{0d,i}(z = 0^-, PAR[Q]) = E_{d,i}(z = 0^-, PAR[Q]) \,/\, \mu_d.$$

Following the observations of Matthes et al. (2019) at the Qikiqtarjuaq ice camp, μ_d was set to 0.6 under snow-covered sea ice and to 0.7 under bare sea ice. The observations of Matthes et al. (2019) also allowed the conversion of $E_{0d,i}(z = 0^-, PAR[Q])$ into the scalar PAR just below sea ice in photon density flux, $E_{0,i}(z = 0^-, PAR[Q])$ (Figure 8b; Data S5 in Benoît-Gagné et al., 2024), as

$$18.\ E_{0,i}(z = 0^-, PAR[Q]) = E_{0d,i}(z = 0^-, PAR[Q])\ 1.03.$$

6.2.2 A2.2 Scalar photosynthetically active radiation below open water

Downwelling shortwave radiation just above surface in energy units, $E_s(z = 0^+, SW)$ (Figure S9a), was from Smith et al. (2014). The processing of $E_s(z = 0^+, SW)$ followed that of the biogeochemical model PISCES (Aumont et al., 2015). The downwelling shortwave radiation just below open water in energy units, $E_s(z = 0^-, SW)$ (Figure S9b), was calculated with an albedo for open water, $\alpha_w = 0.066$, as

$$19.\ E_s(z = 0^-, SW) = E_s(z = 0^+, SW)\ (1 - \alpha_w).$$

The scalar PAR just below open water in energy units, $E_{0,w}(z = 0^-, PAR[W])$ (Figure S9c), was calculated using a factor of 0.43 as

$$20.\ E_{0,w}(z = 0^-, PAR[W]) = E_s(z = 0^-, SW)\ 0.43.$$

The visible spectrum was divided into three equal bands: blue, green and red. The scalar irradiances for each band just below open water in energy units, $E_{0,w,\lambda}(z = 0^-, PAR[W])$ (Figure S9d), were considered equal as

$$21.\ E_{0,w,\lambda=blue}(z = 0^-, PAR[W]) = E_{0,w,\lambda=green}(z = 0^-, PAR[W])$$

$$= E_{0,w,\lambda=red}(z = 0^-, PAR[W]) = E_{0,w}(z = 0^-, PAR[W]) \,/\, 3.$$

The scalar irradiances for each band just below open water in energy units were converted into the scalar irradiances for each band just below open water in photon density flux $E_{0,w,\lambda}(z = 0^-, PAR[Q])$ (Figure S9e), as

$$22.\ E_{0,w,\lambda}(z = 0^-, PAR[Q]) = \frac{E_{0,w}(z=0^-, PAR[W])\ \lambda\ 10^6}{hcN},$$

for λ = blue = 450 nm, λ = green = 550 nm and λ = red = 650 nm. $E_{0,w,\lambda}(z = 0^-, PAR[Q])$ was added up to get the scalar PAR just below open water in photon density flux, $E_{0,w}(z = 0^-, PAR[Q])$ (Figure S9f; Data S5 in Benoît-Gagné et al., 2024), as

$$23.\ E_{0,w}(z = 0^-, PAR[Q]) = \sum_{i=1}^{3} E_{0,w,\lambda_i}(z = 0^-, PAR[Q]).$$

6.2.3 A2.3 Scalar photosynthetically active radiation in the water column

$E_{0,i}(z = 0^-, PAR[Q])$ was used for the forcing field for the scalar PAR just below surface in photon density flux, $E_0(z = 0^-, PAR[Q])$, before sea ice break-up (before July 18). $E_{0,w}(z = 0^-, PAR[Q])$ was used as the forcing field for $E_0(z = 0^-, PAR[Q])$ from the sea ice break-up (from July 18). The water column was divided into 75 depth layers. The scalar PAR at depth *z* in photon density flux was computed with a Beer-Lambert law as

$$24.\ E_0(z, PAR[Q]) = E_0(z = 0^-, PAR[Q]) exp\left(-\int_0^z K_0(z')\, dz'\right),$$

where K_0 was the diffuse vertical attenuation coefficient of scalar PAR. K_0 was dependent on Chl *a* concentration (Chl *a*) as

$$25.\ K_0 = K_w + K_{Chl} Chl\ a,$$

where K_w was light absorption for pure seawater and K_{Chl} was light absorption for Chl *a*. Coloured dissolved organic matter and detrital matter were not considered in the calculation of K_0.

6.3 A3. Adjustments to the observations specific for comparison to the model

The measured PAR was the downwelling plane PAR (E_d), while the model simulated the scalar PAR (E_0). Matthes et al. (2019) found a conversion factor of approximately 1.4 from plane to scalar PAR within the upper 20 m at the Qikiqtarjuaq ice camp. Before June 27, there were observations of Chl *a* only down to 40 m and extrapolation was necessary for the vertical integration to 100 m. Reaching 100 m was required after June 27 because a subsurface chlorophyll maximum was formed by that point. Extrapolation was achieved by considering that Chl *a* below 40 m was equal to Chl *a* at 40 m because, before June 27, Chl *a* remained unchanged with depth (Figure S2d). The depth of the mixing layer was measured during the ice camp only on June 23. The methods for the measurement of the equivalent mixed layer depth (h_{BD}; as in Randelhoff et al., 2017), a measure distinct from the *depth of the mixing layer*, are described in Oziel et al. (2019). The equivalent mixed layer depth was smoothed with a moving average of 7 days.

6.4 A4. Expedition Amundsen *2018*

The relatively deep water depth of 360 m at the ice camp suggested that this site may be representative of offshore western Baffin Bay, even though it was located only a few kilometres from the coast. Data from the 2018 expedition of the Canadian Coast Guard Ship (CCGS) *Amundsen* was used to test this hypothesis. Six stations including one at the Qikiqtarjuaq ice camp location were sampled from July 13 to July 24, 2018 (Leg 2b; Figure S10). Salinity and temperature measurements were acquired with a conductivity-temperature-depth sensor (CTD SBD911plus, SeaBird Scientific). The temperature-salinity diagram for each station showed that the oceanographic conditions in 2018 at the ice camp location (Station 5) were like the oceanographic conditions at the offshore stations (Stations 1 to 3; Figure S11). Thus, we believe that the ice camp location could be considered representative of western Baffin Bay, allowing this modelling study to be representative of this area as well.

6.5 A5. Carbon biomass at the ice camp

The materials and methods for the observation of carbon biomass at the ice camp Qikiqtarjuaq in 2016 is described in Grondin (2019) and Massicotte et al. (2020). Only a brief overview is presented here and illustrated in Figure S12. The 5 ml seawater samples were analysed with an Imaging FlowCytobot (Olson and Sosik, 2007; Sosik and Olson, 2007) manufactured by McLane®. The targeted size range was between 1 µm and 150 µm. Cells larger than 10 µm could be identified to a finer taxonomic resolution than cells between 3 µm and 10 µm due to an image resolution of approximately 3.4 pixels μm^{-1}. The Chl *a* in vivo fluorescence with an excitation laser at 635 nm triggered image acquisition. The resulting greyscale images were processed with a MATLAB (2013b) code (Sosik and Olson, 2007; https://github.com/hsosik/ifcb-analysis, accessed May 29, 2024). This code extracted the regions of interest and their associated features with a random forest algorithm. Each region of interest had 231 features (backscattering, Chl *a*, geometry, shape, symmetry, texture, etc.; see https://github.com/hsosik/ifcb-analysis/wiki/feature-file-documentation, accessed June 11, 2024). These regions and their features were then processed with the EcoTaxa application (Picheral et al., 2017) again using a random forest algorithm. The result was images annotated with one of the 35 taxonomic categories. The annotated images were converted to biovolumes (Moberg and Sosik, 2012). The biovolumes were converted to carbon (Laney and Sosik, 2014) using carbon-to-volume ratios (Menden-Deuer and Lessard, 2000). For the purposes of this study and evaluation of the model, the biomasses of the 35 taxonomic categories were binned into three functional groups: diatoms, mixotrophs and other nanophytoplankton (https://github.com/maximebenoitgagne/timing/blob/main/timing.ipynb, accessed June 11, 2024). Algaebase (Guiry and Guiry, 2022) helped in the classification of the IFCB categories into these groups (Table S8). The "other nanophytoplankton" included strictly autotrophic phytoplankton. More than 99% of the mixotrophs group were dinoflagellates, and as such we refer to this group as "mixotrophic dinoflagellates" in this study.

References

Ardyna, M, Arrigo, KR. 2020. Phytoplankton dynamics in a changing Arctic Ocean. *Nature Climate Change* **10**(10): 892–903. doi: 10.1038/s41558-020-0905-y.

Ardyna, M, Mundy, CJ, Mayot, N, Matthes, LC, Oziel, L, Horvat, C, Leu, E, Assmy, P, Hill, V, Matrai, PA. 2020a. Under-ice phytoplankton blooms: Shedding light on the "invisible" part of Arctic primary production. *Frontiers in Marine Science* **7**: 985. doi: 10.3389/fmars.2020.608032.

Ardyna, M, Mundy, CJ, Mills, MM, Oziel, L, Grondin, P-L, Lacour, L, Verin, G, Van Dijken, G, Ras, J, Alou-Font, E. 2020b. Environmental drivers of under-ice phytoplankton bloom dynamics in the Arctic Ocean. *Elementa: Science of the Anthropocene* **8**. doi: 10.1525/elementa.430.

Aumont, O, Éthé, C, Tagliabue, A, Bopp, L, Gehlen, M. 2015. PISCES-v2: an ocean biogeochemical model for carbon and ecosystem studies. *Geoscientific Model Development* **8**(8): 2465–2513. doi: 10.5194/gmd-8-2465-2015.

Baumgartner, MF, Tarrant, AM. 2017. The physiology and ecology of diapause in marine copepods. *Annual Review of Marine Science* **9**: 387–411. doi: 10.1146/annurev-marine-010816-060505.

Behrenfeld, MJ. 2010. Abandoning Sverdrup's critical depth hypothesis on phytoplankton blooms. *Ecology* **91**(4): 977–989. doi: 10.1890/09-1207.1.

Behrenfeld, MJ, Boss, ES. 2018. Student's tutorial on bloom hypotheses in the context of phytoplankton annual cycles. *Global Change Biology* **24**(1): 55–77. doi: 10.1111/gcb.13858.

Benoît-Gagné, M, Dutkiewicz, S, Deschepper, I, Dufresne, C, Dumont, D, Larouche, R, Mémery, L, Olivier, G, Maps, F. 2024. maximebenoitgagne/timing: Exploring controls on the timing of the phytoplankton bloom in western Baffin Bay, Canadian Arctic (v0.1.4). Zenodo. https://doi.org/10.5281/zenodo.13287110.

Bertin, C, Carroll, D, Menemenlis, D, Dutkiewicz, S, Zhang, H, Matsuoka, A, Tank, S, Manizza, M, Miller, CE, Babin, M, Mangin, A, Le Fouest, V. 2023. Biogeochemical river runoff drives intense coastal Arctic Ocean CO_2 outgassing. *Geophysical Research Letters* **50**(8): e2022GL102377. doi: 10.1029/2022GL102377.

Błachowiak-Samołyk, K, Wiktor, JM, Hegseth, EN, Wold, A, Falk-Petersen, S, Kubiszyn, AM. 2015. Winter Tales: the dark side of planktonic life. *Polar Biology* **38**: 23–36. doi: 10.1007/s00300-014-1597-4.

Boss, E, Behrenfeld, M. 2010. In situ evaluation of the initiation of the North Atlantic phytoplankton bloom. *Geophysical Research Letters* **37**(18). doi: 10.1029/2010GL044174.

Boyd, PW, Claustre, H, Levy, M, Siegel, DA, Weber, T. 2019. Multi-faceted particle pumps drive carbon sequestration in the ocean. *Nature* **568**(7752): 327–335. doi: 10.1038/s41586-019-1098-2.

Carmack, E, Wassmann, P. 2006. Food webs and physical–biological coupling on pan-Arctic shelves: unifying concepts and comprehensive perspectives. *Progress in Oceanography* **71**(2–4): 446–477. doi: 10.1016/j.pocean.2006.10.004.

Castellani, G, Losch, M, Lange, BA, Flores, H. 2017. Modeling Arctic sea-ice algae: Physical drivers of spatial distribution and algae phenology. *Journal of Geophysical Research: Oceans* **122**(9): 7466–7487. doi: 10.1002/2017JC012828.

Christian, JR, Denman, KL, Hayashida, H, Holdsworth, AM, Lee, WG, Riche, OG, Shao, AE, Steiner, N, Swart, NC. 2022. Ocean biogeochemistry in the Canadian Earth system model version 5.0.3: CanESM5 and CanESM5-CanOE. *Geoscientific Model Development Discussions* **15**: 4393–4424. doi: 10.5194/gmd-15-4393-2022.

Cohen, JH, Berge, J, Moline, MA, Johnsen, G, Zolich, AP. 2020. Chapter 3. Light in the Polar Night, in Berge, J, Johnsen, G, Cohen, JH eds., *Polar Night Marine Ecology*. Cham, Switzerland: Springer. (Advances in Polar Ecology, vol. 4). pp. 37–66. doi.org/10.1007/978-3-030-33208-2_3.

Dutkiewicz, S, Boyd, PW, Riebesell, U. 2021. Exploring biogeochemical and ecological redundancy in phytoplankton communities in the global ocean. *Global Change Biology* **27**(6): 1196–1213. doi: 10.1111/gcb.15493.

Dutkiewicz, S, Cermeno, P, Jahn, O, Follows, MJ, Hickman, AE, Taniguchi, DA, Ward, BA. 2020. Dimensions of marine phytoplankton diversity. *Biogeosciences* **17**(3): 609–634. doi: 10.5194/bg-17-609-2020.

Dutkiewicz, S, Hickman, AE, Jahn, O, Gregg, WW, Mouw, CB, Follows, MJ. 2015. Capturing optically important constituents and properties in a marine biogeochemical and ecosystem model. *Biogeosciences* **12**(14): 4447–4481. doi: 10.5194/bg-12-4447-2015.

Follows, MJ, Dutkiewicz, S, Ward, BA, Follet, CN. 2018. Theoretical interpretation of subtropical plankton biogeography, in Gasol, J, Kirshman, D, eds., *Microbial Ecology of the Oceans*. 3rd ed. Hoboken, NJ, USA: John Wiley & Sons, Inc. pp. 467–494.

Frost, BW. 1993. A modelling study of processes regulating plankton standing stock and production in the open subarctic Pacific Ocean. *Progress in Oceanography* **32**(1–4): 17–56. doi: 10.1016/0079-6611(93)90008-2.

Geider, RJ, MacIntyre, HL, Graziano, LM, McKay, RML. 1998. Responses of the photosynthetic apparatus of *Dunaliella tertiolecta* (Chlorophyceae) to nitrogen and phosphorus limitation. *European Journal of Phycology* **33**(4): 315–332. doi: 10.1080/09670269810001736813.

Geider, RJ, MacIntyre, HL, Kana, TM. 1997. Dynamic model of phytoplankton growth and acclimation: responses of the balanced growth rate and the chlorophyll *a*: carbon ratio to light, nutrient-limitation and temperature. *Marine Ecology Progress Series* **148**: 187–200. doi: 10.3354/meps148187.

Geider, RJ, Osbonie, BA, Raven, JA. 1986. Growth, photosynthesis and maintenance metabolic cost in the diatom *Phaeodactylum tricornutum* at very low light levels. *Journal of Phycology* **22**(1): 39–48. doi: 10.1111/j.1529-8817.1986.tb02513.x.

Grondin, P-L. 2019. Rôle des propriétés physiques et chimiques du milieu dans la succession des protistes marins lors de la floraison printanière en baie de Baffin [M.Sc. thesis]. Québec, Québec, Canada: Université Laval, Department of Biology. Available at https://dam-oclc.bac-lac.gc.ca/eng/7949e500-ed1c-4dab-b8a7-d737159bbcd2. Accessed June 10, 2024.

Guiry, MD, Guiry, GM. 2022. AlgaeBase. World-wide electronic publication. Available at https://www.algaebase.org. Accessed May 24, 2022.

Gutiérrez, JM, Jones, RG, Narisma, GT, Muniz Alves, L, Amjad, M, Gorodetskaya, IV, Grose, M, Klutse, NAB, Krakovska, S, Li, J, Martínez-Castro, D, Mearns, LO, Mernild, SH, Ngo-Duc, T, van den Hurk, B, Yoon J-H. 2021. Atlas, in Masson-Delmotte, V, Zhai, P, Pirani, A, Connors, SL, Péan, C, Berger, S, Caud, N, Chen, Y, Goldfarb, L, Gomis, MI, Huang, M, Leitzell, K, Lonnoy, E, Matthews, JBR, Maycock, TK, Waterfield, T, Yelekçi, Ö, Yu, R, Zhou, B, eds., *Climate Change 2021: The Physical Science Basis. Contribution of Working Group I to the Sixth Assessment Report of the Intergovernmental Panel on Climate Change*. Cambridge, UK: Cambridge University Press. pp. 1927–2058. doi: 10.1017/9781009157896.021.

Haddon, A, Farnole, P, Monahan, AH, Sou, T, Steiner, N. 2024. Environmental controls and phenology of sea ice algal growth in a future Arctic. *Elementa: Science of the Anthropocene* **12**(1). doi: 10.1525/elementa.2023.00129.

Hague, M, Vichi, M. 2021. Southern Ocean Biogeochemical Argo detect under-ice phytoplankton growth before sea ice retreat. *Biogeosciences* **18**(1): 25–38. doi: 10.5194/bg-18-25-2021.

Hancke, K, Lund-Hansen, LC, Lamare, ML, Højlund Pedersen, S, King, MD, Andersen, P, Sorrell, BK. 2018. Extreme low light requirement for algae growth underneath sea ice: a case study from station Nord, NE Greenland. *Journal of Geophysical Research: Oceans* **123**(2): 985–1000. doi: 10.1002/2017JC013263.

Handy, J, Juchem, D, Wang, Q, Schimani, K, Skibbe, O, Zimmermann, J, Karsten, U, Herburger, K. 2024. Antarctic benthic diatoms after 10 months of dark exposure: consequences for photosynthesis and cellular integrity. *Frontiers in Plant Science* **15**: 1326375. doi: 10.3389/fpls.2024.1326375.

Hayashida, H, Christian, JR, Holdsworth, AM, Hu, X, Monahan, AH, Mortenson, E, Myers, PG, Riche, OG, Sou, T, Steiner, NS. 2019. CSIB v1 (Canadian Sea-ice Biogeochemistry): A sea-ice biogeochemical model for the NEMO community ocean modelling framework. *Geoscientific Model Development* **12**(5): 1965–1990. doi: 10.5194/gmd-12-1965-2019.

Hayashida, H, Steiner, N, Monahan, A, Galindo, V, Lizotte, M, Levasseur, M. 2017. Implications of sea-ice biogeochemistry for oceanic production and emissions of dimethyl sulfide in the Arctic. *Biogeosciences* **14**(12): 3129–3155. doi: 10.5194/bg-14-3129-2017.

Henson, SA, Briggs, N, Carvalho, F, Manno, C, Mignot, A, Thomalla, S. 2023. A seasonal transition in biological carbon pump efficiency in the northern Scotia Sea, Southern Ocean. *Deep Sea Research Part II: Topical Studies in Oceanography* **208**: 105274. doi: 10.1016/j.dsr2.2023.105274.

Hickman, AE, Dutkiewicz, S, Williams, RG, Follows, MJ. 2010. Modelling the effects of chromatic adaptation on phytoplankton community structure in the oligotrophic ocean. *Marine Ecology Progress Series* **406**: 1–17. doi: 10.3354/meps08588.

Hoppe, CJM. 2022. Always ready? Primary production of Arctic phytoplankton at the end of the polar night. *Limnology and Oceanography Letters* **7**(2): 167–174. doi: 10.1002/lol2.10222.

Jakobsson, M, Mayer, L, Coakley, B, Dowdeswell, JA, Forbes, S, Fridman, B, Hodnesdal, H, Noormets, R, Pedersen, R, Rebesco, M. 2012. The international bathymetric chart of the Arctic Ocean (IBCAO) version 3.0. *Geophysical Research Letters* **39**(12). doi: 10.1029/2012GL052219.

Jeong, HJ, Yoo, YD, Kim, JS, Seong, KA, Kang, NS, Kim, TH. 2010. Growth, feeding and ecological roles of the mixotrophic and heterotrophic dinoflagellates in marine planktonic food webs. *Ocean Science Journal* **45**(2): 65–91. doi: 10.1007/s12601-010-0007-2.

Johnsen, G, Leu, E, Gradinger, R. 2020. Chapter 4. Marine micro- and macroalgae in the Polar Night, in Berge, J, Johnsen, G, Cohen, JH, eds., *Polar Night Marine Ecology*. Cham, Switzerland: Springer. (Advances in Polar Ecology, vol. 4). pp. 67–112. doi.org/10.1007/978-3-030-33208-2_4.

Joli, N, Concia, L, Mocaer, K, Guterman, J, Laude, J, Guerin, S, Sciandra, T, Bruyant, F, Ait-Mohamed, O, Beguin, M, Forget, M, Bourbousse, C, Lacour, T, Bailleul, B, Nef, C, Savoie, M, Tremblay, J, Campbell, DA, Lavaud, J, Schwab, Y, Babin, M, Bowler, C. 2024. Hypometabolism to survive the long polar night and subsequent successful return to light in the diatom *Fragilariopsis cylindrus*. *New Phytologist* **241**(5): 2193–2208. doi: 10.1111/nph.19387.

Kennedy, F, Martin, A, Bowman, JP, Wilson, R, McMinn, A. 2020. Dark metabolism: a molecular insight into how the Antarctic sea-ice diatom *Fragilariopsis cylindrus* survives long-term darkness. *New Phytologist* **223**(2): 675–691. doi: 10.1111/nph.15843.

Kenny, T-A, Chan, HM. 2017. Estimating wildlife harvest based on reported consumption by Inuit in the Canadian Arctic. *Arctic* **70**(1): 1–12.

Kuhn, AM, Mazloff, M, Dutkiewicz, S, Jahn, O, Clayton, S, Rynearson, T, Barton, AD. 2023. A global comparison of marine chlorophyll variability observed in Eulerian and Lagrangian perspectives. *Journal of Geophysical Research: Oceans* **128**(7): 1–12. doi: 10.1029/2023JC019801.

Kvernvik, AC, Hoppe, CJM, Lawrenz, E, Prášil, O, Greenacre, M, Wiktor, JM, Leu, E. 2018. Fast reactivation of photosynthesis in arctic phytoplankton during the polar night. *Journal of Phycology* **54**(4): 461–470. doi: 10.1111/jpy.12750.

Lacour, T, Morin, P-I, Sciandra, T, Donaher, N, Campbell, DA, Ferland, J, Babin, M. 2019. Decoupling light harvesting, electron transport and carbon fixation during prolonged darkness supports rapid recovery upon re-illumination in the Arctic diatom *Chaetoceros neogracilis*. *Polar Biology* **42**(10): 1787–1799. doi: 10.1007/s00300-019-02507-2.

Laney, SR, Sosik, HM. 2014. Phytoplankton assemblage structure in and around a massive under-ice bloom in the Chukchi Sea. *Deep Sea Research Part II: Topical Studies in Oceanography* **105**: 30–41. doi: 10.1016/j.dsr2.2014.03.012.

Lavoie, M, Waller, JC, Kiene, RP, Levasseur, M. 2018. Polar marine diatoms likely take up a small fraction of dissolved dimethylsulfoniopropionate relative to bacteria in oligotrophic environments. *Aquatic Microbial Ecology* **81**(3): 213–218. doi: 10.3354/ame01871.

Legendre, L, Rassoulzadegan, F. 1995. Plankton and nutrient dynamics in marine waters. *Ophelia* **41**(1): 153–172. doi: 10.1080/00785236.1995.10422042.

Letelier, RM, Karl, DM, Abbott, MR, Bidigare, RR. 2004. Light driven seasonal patterns of chlorophyll and nitrate in the lower euphotic zone of the North Pacific Subtropical Gyre. *Limnology and Oceanography* **49**(2): 508–519. doi: 10.4319/lo.2004.49.2.0508.

Leu, E, Søreide, JE, Hessen, DO, Falk-Petersen, S, Berge, J. 2011. Consequences of changing sea-ice cover for primary and secondary producers in the European Arctic shelf seas: timing, quantity, and quality. *Progress in Oceanography* **90**(1–4): 18–32. doi: 10.1016/j.pocean.2011.02.004.

Madec, G, Bourdallé-Badie, R, Bouttier, P-A, Bricaud, C, Bruciaferri, D, Calvert, D, Chanut, J, Clementi, E, Coward, A, Delrosso, D, Ethé, C, Flavoni, S, Graham, T, Harle, J, Iovino, D, Lea, D, Lévy, C, Lovato, T, Martin, N, Masson, S, Mocavero, S, Paul, J, Rousset, C, Storkey, D, Storto, A, Vancoppenolle, M. 2017. NEMO ocean engine in *Notes du Pôle de modélisation de l'Institut Pierre-Simon Laplace (IPSL)* (v3.6-patch, Number 27**)**. Zenodo. https://doi.org/10.5281/zenodo.3248739.

Marquardt, M, Vader, A, Stübner, EI, Reigstad, M, Gabrielsen, TM. 2016. Strong seasonality of marine microbial eukaryotes in a High-Arctic fjord (Isfjorden, in West Spitsbergen, Norway). *Applied and Environmental Microbiology* **82**(6): 1868–1880. doi: 10.1128/AEM.03208-15.

Massicotte, P, Amiraux, R, Amyot, M-P, Archambault, P, Ardyna, M, Arnaud, L, Artigue, L, Aubry, C, Ayotte, P, Bécu, G, Bélanger, S, Benner, R, Bittig, HC, Bricaud, A, Brossier, É, Bruyant, F, Chauvaud, L, Christiansen-Stowe, D, Claustre, H, Cornet-Barthaux, V, Coupel, P, Cox, C, Delaforge, A, Dezutter, T, Dimier, C, Dominé, F, Dufour, F, Dufresne, C, Dumont, D, Ehn, J, Else, B, Ferland J, Forget, M-H, Fortier, L, Galí, M, Galindo, V, Gallinari, M, Garcia, N, Gérikas-Ribeiro, C, Gourdal, M, Gourvil, P, Goyens, C, Grondin, P-L, Guillot, P, Guilmette, C, Houssais, M-N, Joux, F, Lacour, L, Lacour, T, Lafond, A, Lagunas, J, Lalande, C, Laliberté, J, Lambert-Girard, S, Larivière, J, Lavaud, J, LeBaron, A, Leblanc, K, Le Gall, F, Legras, J, Lemire, M, Levasseur, M, Leymarie, E, Leynaert, A, Lopes dos Santos, A, Lourenço, A, Mah, D, Marec, C, Marie, D, Martin, N, Marty, C, Marty, S, Massé, G, Matsuoka, A, Matthes, L, Moriceau, B, Muller, P-E, Mundy, CJ, Neukermans, G, Oziel, L, Panagiotopoulos, C, Pangazi, J-J, Picard, G, Picheral, M, Pinczon du Sel, F, Pogorzelec, N, Probert, I, Queguiner, B, Raimbault, P, Ras, J, Rehm, E, Reimer, E, Rontani, J-F, Rysgaard, S, Saint-Béat, B, Sampei, M, Sansoulet, J, Schmechtig, C, Schmidt, S, Sempéré, R, Sévigny, C, Shen, Y, Tragin, M, Tremblay, J-É, Vaulot, D, Verin, G, Vivier, F, Vladoiu, A, Whitehead, J, Babin, M. 2020. Green Edge ice camp campaigns: understanding the processes controlling the under-ice Arctic phytoplankton spring bloom. *Earth System Science Data* **12**(1): 151–176. doi: 10.5194/essd-12-151-2020.

Massicotte, P, Amiraux, R, Amyot, M-P, Archambault, P, Ardyna, M, Arnaud, L, Artigue, L, Aubry C, Ayotte, P, Bécu, G, Bélanger, S, Benner, R, Bittig, HC, Bricaud, A, Brossier, É, Bruyant, F, Chauvaud, L, Christiansen-Stowe, D, Claustre, H, Cornet-Barthaux, V, Coupel, P, Cox C, Delaforge, A, Dezutter, T, Dimier, C, Dominé, F, Dufour, F, Dufresne, C, Dumont, D, Ehn, J, Else, B, Ferland, J, Forget, M-H, Fortier, L, Galí, M, Galindo, V, Gallinari, M, Garcia, N, Gérikas-Ribeiro, C, Gourdal, M, Gourvil, P, Goyens, C, Grondin, P-L, Guillot, P, Guilmette, C, Houssais, M-N, Joux, F, Lacour, L, Lacour, T, Lafond, A, Lagunas, J, Lalande, C, Laliberté, J, Lambert-Girard, S, Larivière, J, Lavaud, J, LeBaron, A, Leblanc, K, Le Gall, F, Legras, J, Lemire, M, Levasseur, M, Leymarie, E, Leynaert, A, Lopes dos Santos, A, Lourenço, A, Mah, D, Marec, C, Marie, D, Martin, N, Marty, C, Marty, S, Massé, G, Matsuoka, A, Matthes, L, Moriceau, B, Muller, P-E, Mundy, CJ, Neukermans, G, Oziel, L, Panagiotopoulos, C, Pangazi, J-J, Picard, G, Picheral, M, Pinczon du Sel, F, Pogorzelec, N, Probert, I, Queguiner, B, Raimbault, P, Ras, J, Rehm, E, Reimer, E, Rontani, J-F, Rysgaard, S, Saint-Béat, B, Sampei, M, Sansoulet, J, Schmidt, S, Sempéré, R, Sévigny, C, Shen, Y, Tragin, M, Tremblay, J-É, Vaulot, D, Verin, G, Vivier, F, Vladoiu, A, Whitehead, J, Babin, M. 2019. The Green Edge initiative: understanding the processes controlling the under-ice Arctic phytoplankton spring bloom. *SEANOE*. doi: 10.17882/59892.

Matthes, LC, Ehn, JK, L-Girard, S, Pogorzelec, NM, Babin, M, Mundy, CJ, Arrigo, K. 2019. Average cosine coefficient and spectral distribution of the light field under sea ice: Implications for primary production. *Elementa: Science of the Anthropocene* **7**. doi: 10.1525/elementa.363.

Mayot, N, Matrai, P, Ellingsen, IH, Steele, M, Johnson, K, Riser, SC, Swift, D. 2018. Assessing phytoplankton activities in the seasonal ice zone of the Greenland Sea over an annual cycle. *Journal of Geophysical Research: Oceans* **123**(11): 8004–8025. doi: 10.1029/2018JC014271.

Menden-Deuer, S, Lessard, EJ. 2000. Carbon to volume relationships for dinoflagellates, diatoms, and other protist plankton. *Limnology and Oceanography* **45**(3): 569–579. doi: 10.4319/lo.2000.45.3.0569.

Moberg, EA, Sosik, HM. 2012. Distance maps to estimate cell volume from two-dimensional plankton images. *Limnology and Oceanography: Methods* **10**(4): 278–288. doi: 10.4319/lom.2012.10.278.

Morin, P-I, Lacour, T, Grondin, P-L, Bruyant, F, Ferland, J, Forget, M-H, Massicotte, P, Donaher, N, Campbell, DA, Lavaud, J. 2020. Response of the sea-ice diatom Fragilariopsis cylindrus to simulated polar night darkness and return to light. *Limnology and Oceanography* **65**(5): 1041–1060. doi: 10.1002/lno.11368.

Mortenson, E, Hayashida, H, Steiner, N, Monahan, A, Blais, M, Gale, MA, Galindo, V, Gosselin, M, Hu, X, Lavoie, D. 2017. A model-based analysis of physical and biological controls on ice algal and pelagic primary production in Resolute Passage. *Elementa: Science of the Anthropocene* **5**. doi: 10.1525/elementa.229.

Mortenson, E, Steiner, N, Monahan, AH, Miller, LA, Geilfus, N-X, Brown, K. 2018. A model-based analysis of physical and biogeochemical controls on carbon exchange in the upper water column, sea ice, and atmosphere in a seasonally ice-covered Arctic strait. *Journal of Geophysical Research: Oceans* **123**(10): 7529–7549. doi: 10.1029/2018JC014376.

Olson, RJ, Sosik, HM. 2007. A submersible imaging-in-flow instrument to analyze nano-and microplankton: Imaging FlowCytobot. *Limnology and Oceanography: Methods* **5**(6): 195–203. doi: 10.4319/lom.2007.5.195.

Oziel, L, Massicotte, P, Randelhoff, A, Ferland, J, Vladoiu, A, Lacour, L, Galindo, V, Lambert-Girard, S, Dumont, D, Cuypers, Y. 2019. Environmental factors influencing the seasonal dynamics of spring algal blooms in and beneath sea ice in western Baffin Bay. *Elementa: Science of the Anthropocene* **7**. doi: 10.1525/elementa.372.

Perrette, M, Yool, A, Quartly, GD, Popova, EE. 2011. Near-ubiquity of ice-edge blooms in the Arctic. *Biogeosciences* **8**(2): 515–524. doi: 10.5194/bg-8-515-2011.

Picheral, M, Colin, S, Irisson, J-O. 2017. EcoTaxa, a tool for the taxonomic classification of images. Available at https://ecotaxa.obs-vlfr.fr/. Accessed May 29, 2024.

Randelhoff, A, Fer, I, Sundfjord, A. 2017. Turbulent upper-ocean mixing affected by meltwater layers during Arctic summer. *Journal of Physical Oceanography* **47**(4): 835–853. doi: 10.1175/JPO-D-16-0200.1.

Randelhoff, A, Lacour, L, Marec, C, Leymarie, E, Lagunas, J, Xing, X, Darnis, G, Penkerc'h, C, Sampei, M, Fortier, L. 2020. Arctic mid-winter phytoplankton growth revealed by autonomous profilers. *Science Advances* **6**(39): eabc2678. doi: 10.1126/sciadv.abc2678.

Randelhoff, A, Oziel, L, Massicotte, P, Bécu, G, Galí, M, Lacour, L, Dumont, D, Vladoiu, A, Marec, C, Bruyant, F. 2019. The evolution of light and vertical mixing across a phytoplankton ice-edge bloom. *Elementa: Science of the Anthropocene* **7**. doi: 10.1525/elementa.357.

Rantanen, M, Karpechko, AY, Lipponen, A, Nordling, K, Hyvärinen, O, Ruosteenoja, K, Vihma, T, Laaksonen, A. 2022. The Arctic has warmed nearly four times faster than the globe since 1979. *Communications Earth & Environment* **3**(1): 168. doi: 10.1038/s43247-022-00498-3.

Rose, JM, Caron, DA. 2007. Does low temperature constrain the growth rates of heterotrophic protists? Evidence and implications for algal blooms in cold waters. *Limnology and Oceanography* **52**(2): 886–895. doi: 10.4319/lo.2007.52.2.0886.

Rousset, C, Vancoppenolle, M, Madec, G, Fichefet, T, Flavoni, S, Barthélemy, A, Benshila, R, Chanut, J, Lévy, C, Masson, S. 2015. The Louvain-La-Neuve sea ice model LIM3.6: global and regional capabilities. *Geoscientific Model Development* **8**(10): 2991–3005. doi: 10.5194/gmd-8-2991-2015.

Sakshaug, E. 2004. Primary and Secondary Production in the Arctic Seas, in Stein, R, MacDonald, RW, eds., *The Organic Carbon Cycle in the Arctic Ocean*. Berlin and Heidelberg, Germany: Springer-Verlag. pp. 57–81. Available at https://link.springer.com/book/10.1007/978-3-642-18912-8.

Sakshaug, E, Slagstad, D, Holm-Hansen, O. 1991. Factors controlling the development of phytoplankton blooms in the Antarctic Ocean—a mathematical model. *Marine Chemistry* **35**(1–4): 259–271. doi: 10.1016/S0304-4203(09)90021-4.

Smith, GC, Roy, F, Mann, P, Dupont, F, Brasnett, B, Lemieux, J-F, Laroche, S, Bélair, S. 2014. A new atmospheric dataset for forcing ice–ocean models: Evaluation of reforecasts using the Canadian global deterministic prediction system. *Quarterly Journal of the Royal Meteorological Society* **140**(680): 881–894. doi: 10.1002/qj.2194.

Søreide, JE, Leu, EV, Berge, Jør, Graeve, M, Falk-Petersen, S. 2010. Timing of blooms, algal food quality and *Calanus glacialis* reproduction and growth in a changing Arctic. *Global Change Biology* **16**(11): 3154–3163. doi: 10.1111/j.1365-2486.2010.02175.x.

Sosik, HM, Olson, RJ. 2007. Automated taxonomic classification of phytoplankton sampled with imaging-in-flow cytometry. *Limnology and Oceanography: Methods* **5**(6): 204–216. doi: 10.4319/lom.2007.5.204.

Stoecker, DK, Lavrentyev, PJ. 2018. Mixotrophic plankton in the polar seas: A pan-arctic review. *Frontiers in Marine Science* **5**: 292. doi: 10.3389/fmars.2018.00292.

Taniguchi, DA, Landry, MR, Franks, PJ, Selph, KE. 2014. Size-specific growth and grazing rates for picophytoplankton in coastal and oceanic regions of the eastern Pacific. *Marine Ecology Progress Series* **509**: 87–101. doi: 10.3354/meps10895.

Vader, A, Marquardt, M, Meshram, AR, Gabrielsen, TM. 2015. Key Arctic phototrophs are widespread in the polar night. *Polar Biology* **38**(1): 13–21. doi: 10.1007/s00300-014-1570-2.

Wassmann, P, Reigstad, M. 2011. Future Arctic Ocean seasonal ice zones and implications for pelagic-benthic coupling. *Oceanography* **24**(3): 220–231. doi: 10.5670/oceanog.2011.74.

Wen, Z-Y, Jiang, Y, Chen, F. 2002. High cell density culture of the diatom *Nitzschia laevis* for eicosapentaenoic acid production: fed-batch development. *Process Biochemistry* **37**(12): 1447–1453. doi: 10.1016/S0032-9592(02)00034-1.

Wu, Z, Dutkiewicz, S, Jahn, O, Sher, D, White, A, Follows, MJ. 2021. Modeling photosynthesis and exudation in subtropical oceans. *Global Biogeochemical Cycles* **35**(9): 1–14. doi: 10.1029/2021GB006941.

Contributions

Conception and design: MBG, SD, FM.

Analysed data: MBG.

Interpreted data: MBG, SD, ID, CD, DD, LM, FM.

Acquisition and processing of temperature and salinity data during the CCGS Amundsen 2018 expedition: RL.

Processing of nutrient concentrations before May 15 from the Qikiqtarjuaq sea ice camps 2015 and 2016: GO.

NEMO-LIM3 modelling to provide offline physical forcing fields (temperature, salinity and mixing) for the MITgcm modelling: GO.

MITgcm modelling: MBG.

Manuscript preparation: MBG, RL, GO.

Critical review and revision of the manuscript: MBG, SD, ID, CD, DD, LM, FM.

Final approval of the versions to be submitted: MBG, SD, ID, CD, DD, RL, LM, GO, FM.

Acknowledgements

We thank Joannie Ferland and Marie-Hélène Forget for organising the Qikiqtarjuaq ice camps. We thank Virginie Galindo for snow and ice thickness, Guislain Bécu and Marcel Babin for PAR, Patrick Raimbault for nitrate and silicic acid concentrations, Joséphine Ras and Hervé Claustre for high-performance liquid chromatography analyses, Joannie Ferland, Pierre-Luc Grondin and Marcel Babin for IFCB analyses and all other scientists and technicians who contributed to fieldwork. MBG thanks Jean-Michel Campin, Oliver Jahn and Jeffery Scott for their help in mastering the code of MITgcm. MBG thanks Achim Randelhoff for useful code examples (https://github.com/poplarShift/ice-edge). MBG thanks Yannick Copin for a useful code example of a Taylor diagram (https://gist.github.com/ycopin/3342888). MBG thanks Arthur Plassart and Sarah Schembri for suggestions on the manuscript.

Funding information

This research was funded by the Sentinel North program of Université Laval, funded by the Canada First Research Excellence Fund. The GreenEdge project was conducted under the scientific coordination of the CERC program and of the CNRS & Université Laval Takuvik International Research Laboratory (LRI3376). The GreenEdge project was funded by the following French and Canadian programs and agencies: ANR (Contract #111112), ArcticNet, CERC on Remote sensing of Canada's new Arctic frontier, CNES (project #131425), French Arctic Initiative, Fondation Total, CSA, LEFE and IPEV (project #1164). The Amundsen 2018 cruise was conducted using the Canadian research icebreaker

CCGS *Amundsen* with the support of the Amundsen Science program funded by the Canada Foundation for Innovation (CFI) Major Science Initiatives Fund. The supercomputing infrastructure was provided by the Digital Research Alliance of Canada. MBG acknowledges Sentinel North for a doctoral scholarship. MBG acknowledges the Fonds de Recherche du Québec and the Sentinel North program for funding a research appointment at the Massachusetts Institute of Technology, Cambridge, MA, USA. MBG acknowledges the Fonds de Recherche du Québec for funding a research appointment at the Laboratoire des Sciences de l'Environnement Marin (CNRS), Plouzané, France. This work is a contribution to the scientific program of the interinstitutional research group Québec-Océan. CD was supported by a grant from the Weston Family Foundation awarded to FM. SD acknowledges the support of NASA Earth Science Division's Interdisciplinary Science (IDS) program (grant number 80NM0018D0004). DD was supported by NSERC Discovery Grants (RGPIN-2013-402257, RGPIN-2019-06563). RL acknowledges the support of the SMAART program through the Collaborative Research and Training Experience program (CREATE) of the NSERC. FM was supported by NSERC Discovery Grants (RGPIN-2014-05433, RGPIN-2021-03876).

Competing interest

The authors have declared that no competing interests exist.

Supplemental material

The file supplement.docx has been submitted with the present article. It contains the following supplemental figures and tables.

- **Figure S1.** Photosynthetic parameters.
- **Figures S2.** Nutrient concentrations and chlorophyll *a*.
- **Figures S3.** Accumulation rate.
- **Figures S4.** Sensitivity simulations by phytoplankton groups and size classes: EXP-1 prescribed minimum biomass.
- **Figures S5.** Sensitivity simulations by phytoplankton groups and size classes: EXP-2 with differing light under sea ice.
- **Figures S6**. Sensitivity simulations by phytoplankton groups and size classes: EXP-3 prescribed pre-bloom nitrate concentrations.
- **Figure S7.** Mean biomass and chlorophyll *a* (0-40m).
- **Figure S8.** Parameters controlling the half saturation for growth on nitrate for each numerical type.
- **Figures S9.** Processing of downwelling shortwave radiation just above the surface.
- **Figure S10.** Maps of Baffin Bay and the study site including the expedition *Amundsen* 2018.

- **Figure S11.** Observations of temperature and salinity during the expedition *Amundsen* 2018.
- **Figure S12.** Materials and methods for the observation of the carbon biomass at the ice camp Qikiqtarjuaq 2016.
- **Figure S13.** Annual drift of nitrate.
- **Table S1.** Notations mentioned in the Main Text.
- **Table S2.** Features of the phytoplankton blooms at the Qikiqtarjuaq ice camps in 2015 and 2016.
- **Table S3.** Notations mentioned in the Appendix A1.
- **Table S4.** Constants and fixed parameters mentioned in the Appendix A1.
- **Table S5.** Coefficients for allometric scaling (unitless) mentioned in Appendix A1.
- **Table S6.** Notations mentioned in the Appendix A2.
- **Table S7.** Constants and fixed parameters mentioned in the Appendix A2.
- **Table S8.** Classification of the Imaging FlowCytobot (IFCB) taxonomic categories into the biogeochemical groups of the model.

Data Accessibility Statement

Model output and other data for the generation of the figures are openly accessible in the data directory at https://github.com/maximebenoitgagne/timing/tree/v0.1.4 (Benoît-Gagné et al., 2024). DOI: https://doi.org/10.5281/zenodo.13287110.

The physical model used here is available through http://mitgcm.org/, and the generic ecosystem used in this study is available through https://gud.mit.edu/git/gud. The specific modifications for the setup used here, the code for the new options to the ecosystem code, all parameters values, and the code to generate the figures are provided at https://github.com/maximebenoitgagne/timing/tree/v0.1.4 (Benoît-Gagné et al., 2024). DOI: https://doi.org/10.5281/zenodo.13287110. The code to generate the figures can be visualised by opening the file timing.ipynb. The code to generate the supplemental figures can be visualised by opening the file timing_supmat.ipynb.